

MID-INFRARED IMAGING SPECTROSCOPY OF N₂O SOLID SIMULATING THE HAZE OF TRANS-NEPTUNIAN OBJECTS

Daiki Takama^{1*} 

Ryoichi Koga² 

Shohei Negishi³ , Biao Zhao³ , Yuan Li³ , Yasuhiro Hirahara³ 

Fumiyuki Ito⁴ 

April 4, 2025

ABSTRACT

Nitrous oxide (N₂O) ice is likely to exist in trans-Neptunian objects such as Pluto and Triton, potentially formed through ultraviolet (UV) radiation from the Sun or cosmic ray irradiation of N₂ and CO ices. However, the mid-infrared spectral characteristics of N₂O ice in higher temperature regions (90-110 K), changes in mid-infrared spectra during UV irradiation, and the chemical network of nitrogen oxide (N_xO_y) ices remain insufficiently understood. This study aims to elucidate these aspects through in-situ mid-infrared spectral measurements of cryogenic particles using two-dimensional imaging Fourier transform infrared spectroscopy.

Spectroscopic imaging confirmed strong absorption at 7.75 μm (N₂O ν₁ vibrational mode), with weaker vibrational modes observed at 8.60 μm (N₂O 2ν₂), 7.27 μm (N₂O torsion), and 5.29 μm (N₂O ν₁+ν₂). Annealing experiments simulating high-temperature conditions demonstrated that all vibrational modes irreversibly intensified with increasing temperature, indicating progressive crystallization. New spectral features appeared at approximately 12 μm and 14 μm at the condensed sample.

N₂O ice was exposed to ultraviolet radiation (190-340 nm) using a D₂ lamp for 8.5 hours to investigate spectral changes during UV irradiation. After 60-90 minutes of irradiation, all N₂O vibrational modes disappeared, while absorption intensities of various nitrogen oxides, including NO, NO₂, N₂O₃, and O₃ increased. Beyond 180 minutes, vibrational modes of multiple nitrogen oxide ices exhibited intensity variations across different wavelengths, corresponding to other species such as cis-(NO)₂, N₂O₄, and N₂O₅.

Keywords trans-Neptunian objects, N₂O ice, surface, atmosphere, mid-infrared Imaging Spectroscopy, annealing, UV irradiation, Low-temperature solid-state chemistry.

1 Background

Nitrous oxide (N_2O) is a crucial substance for generating life precursor amino acids, with its solid form at low temperatures creating a molecular crystal through strong electrostatic interactions due to significant molecular polarization. These prebiotic amino acids form through the dissociation and recombination of nitrogen compounds, with N_2O functioning as an essential seed material in this formation process (Bergantini et al. 2022a).

Despite extensive spectroscopic observations of various planetary surfaces, atmospheres, and interstellar ice dust (Boduch et al. 2015; Allodi et al. 2013), infrared spectra of N_2O ice remain unreported. The vibrational spectra of N_2O ice in the infrared region likely exhibit complex responses due to solid particle growth, metamorphism, and photodissociation processes triggered by solar ultraviolet (UV) radiation.

Previous observations by planetary exploration satellites Voyager 2 and New Horizons have revealed geologically active cryovolcanoes on Pluto and Triton (Grundy et al. 2016). Portions of these surfaces feature geysers emitting nitrogen compounds (Schenk et al. 2021; Singer et al. 2022). Research suggests that N_2O ice forms on the surfaces and in the atmospheres of Pluto and Triton when N_2 interacts with CO , CO_2 , and O_2 under exposure to UV radiation and cosmic rays (Equation 1) (Jamieson et al. 2005; Almeida et al. 2017).



As shown in Figure 1, Voyager 2, New Horizons, and ALMA telescope data have enabled predictions of temperature and pressure distributions relative to altitude, as well as number densities of N_2 ice on Pluto and Triton. Strobel and Zhu 2017 predicted these celestial bodies maintain tenuous atmospheres with temperatures ranging from approximately 38 K (surface) to 110 K (at altitudes of several tens of km) and pressures between 10^{-1} and 10^{-2} Pa. Previous studies have attempted environmental simulation spectroscopic observations of N_2O ice in the infrared spectrum.

Mifsud et al. 2022 irradiated N_2O ice at 20 K and 10^{-4} Pa with 5 keV electrons simulating cosmic radiation, resulting in the formation of N_2O_4 and O_3 ice in both crystalline and amorphous phases. They observed different intensity ratios between the ν_1 and $2\nu_2$ modes in crystalline versus amorphous phases, with the amorphous phase exhibiting lower intensities than the crystalline phase.

Barros et al. 2017 measured transmission absorption spectra of N_2O ice between 10 K and 80 K in the mid-infrared wavelength region corresponding to fundamental vibrational absorptions of N_2O molecules. From 10 K to 40 K, absorbance of ν_1 (symmetric stretching), $2\nu_2$ (antisymmetric stretching), and ν_3 (bending) vibrations increased as crystallization progressed. Subsequently, these vibrations showed decreased absorbance from 40 K to 80 K as the sublimation curve was exceeded.

Hudson et al. 2017 first measured band strengths and absorption coefficients of amorphous and crystalline N_2O ice. They emphasized that temperature and deposition rate are crucial in N_2O ice formation. Increasing deposition thickness from 0.04 to 0.16 μm at 10 K and 10^{-6} Pa revealed clearer spectral structures of amorphous phase vibrations: ν_3 (bending) at 4.47 μm , ν_1 (symmetric stretching) at 7.73 μm , and ν_2 (antisymmetric stretching) at 16.9 μm . Maintaining a constant deposition thickness of 0.18 μm while warming from 10 K to 70 K induced a phase transition from amorphous to crystalline between 24 K and 37 K.

These various environmental simulation spectroscopy experiments have yielded diverse insights into N_2O ice formation processes and behaviors. However, since New Horizons observations (Singer et al. 2022), no mid-infrared spectroscopic observations have simulated high-temperature regions above 10 km altitude (90 K - 110 K) where materials erupt from cryovolcanoes on Pluto and Triton. Furthermore, the relationship between chemical evolution processes induced by UV radiation and vibrational spectra in the infrared region remains unclear.

One approach involves infrared spectroscopy experiments on N_2O ice simulating Pluto and Triton's surface and atmospheric conditions. While obtaining solid-state information in the radio region corresponding to rotational transitions is theoretically impossible due to constrained molecular rotation in solids, the infrared region corresponding to vibration-rotation transitions allows simultaneous acquisition of gas and solid information. Our study represents the first attempt to obtain mid-infrared spectroscopic data in higher temperature regions and to clarify spectral changes induced by simulated solar UV radiation, offering significant scientific value. Predicting N_2O ice chemical networks under solar UV radiation will also facilitate comparisons with future planetary exploration satellite observations.

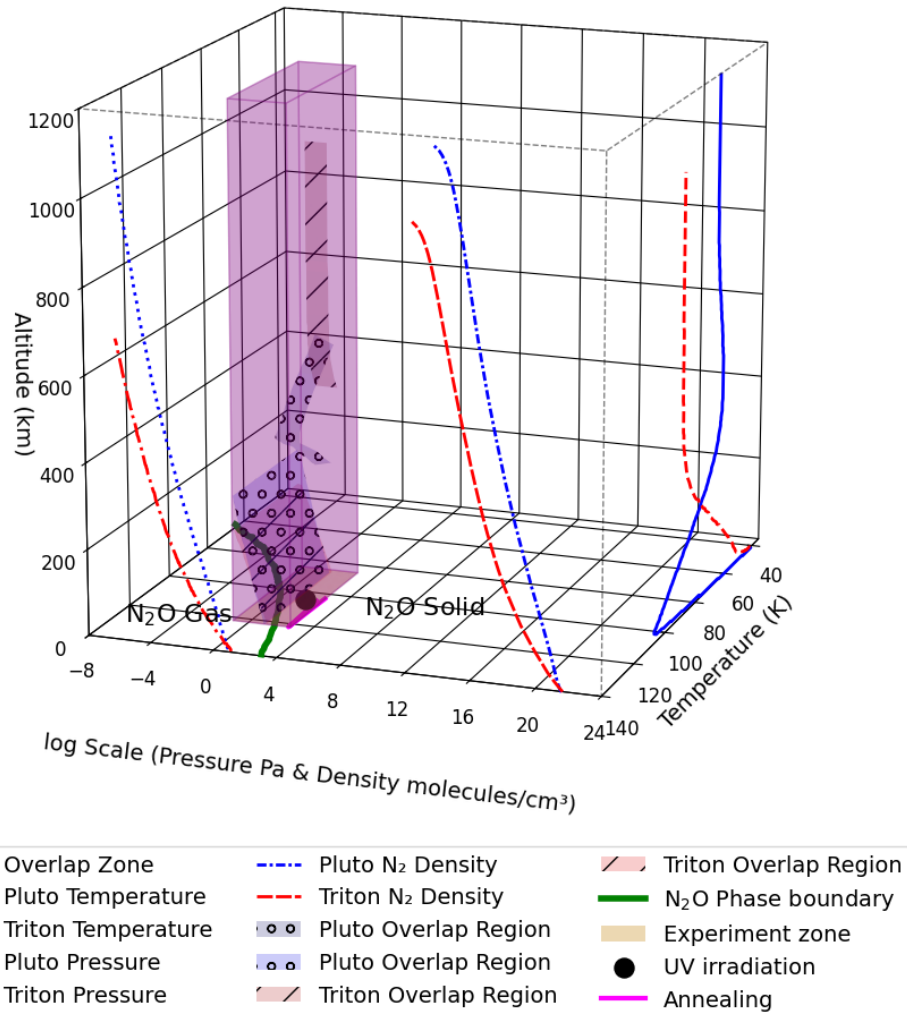


Figure 1: Temperature, pressure, and nitrogen ice number density distributions for altitude for Pluto and Triton (Strobel and Zhu 2017). The pink region indicates the temperature and pressure conditions simulated in this study. The green line on the bottom surface represents the phase boundary of N₂O (Ferreira and Lobo 2009). The temperature and pressure range during annealing and UV irradiation in this experiment are indicated by pink lines and black dots. Additionally, each celestial body's intersection regions of pressure and temperature are represented as dotted areas within the pink region (Overlap Region).

2 Methods

2.1 Experimental equipment

The 2D FT-MIR operates based on a quasi-common-path wavefront-division phase-shifting interferometry method (Qi et al. 2015), which introduces spatial phase differences through wavefront division and amplifies interference light components at the imaging plane for detection.

A mid-infrared light source (SLS303, Thorlabs Co., $0.55 \mu\text{m} < \lambda < 15 \mu\text{m}$), a cryostat with vacuum chamber, and a 2D FT-MIR spectrometer (NK-0812-TD-NU, Nisshin Machinery Co., wavelength range $8 \mu\text{m} < \lambda < 12 \mu\text{m}$, wavelength resolution $\Delta\lambda$ 0.5 μm) are aligned linearly to measure the growth and metamorphism processes of N_2O ice through mid-infrared transmission absorption imaging spectroscopy (Figure 2) (Koga et al. 2024).

The mid-infrared light source irradiates the sample holder perpendicularly with mid-infrared radiation. ZnSe aspheric lenses serve as the incident and exit windows on the vacuum chamber walls, with focal lengths of 63.5 mm and 25 mm, respectively. By setting the distance from the sample holder to the exit ZnSe lens at 52.5 mm and the distance from the exit ZnSe lens to the 2D FT-MIR multi-slit at 44.5 mm, the N_2O sample can be observed at unity magnification on the 2D FT-MIR detector.

2.2 Procedure

Initially, the vacuum chamber is purged with nitrogen, followed by approximately one hour of baking. This baking process prevents corrosion inside the vacuum chamber by removing water, carbon dioxide, and compounds such as nitric acid. Residual gases in the vacuum chamber without deposition and gases generated from sublimated N_2O solid samples are evacuated through a vacuum bellow rough pumping port equipped with a liquid nitrogen trap in the release path. This evacuation utilizes a pump with corrosion-resistant oil (PD-52, ULVAC).

Subsequently, the main vacuuming port valve on the vacuum chamber wall is opened. A backing dry scroll pump (IDP-3, Agilent Technologies) operates for approximately 15 minutes, followed by a main vacuuming dry turbo molecular pump (Agilent TwisTorr 74 FS, Agilent Technologies) running for about 1 hour to depressurize the vacuum chamber. Next, a few drops of ethanol are added to the interior of the Dewar bottle before filling it with liquid nitrogen to cool the sample holder with a ZnSe plate connected to the cold head. Aluminum tape is applied to a 2 mm wide groove on the upper part of the sample holder, employing the Thermal anchor method to reduce heat influx from the external environment. Silver paste is applied to the contact area of the cold head, and aluminum retaining screws are used to enhance thermal conductivity. The sample holder temperature is reduced to approximately 85 K, and the pressure inside the vacuum chamber is decreased to $10^{-2} \sim 10^{-3}$ Pa.

Next, N_2O standard gas (99.9 % purity, 10 L, Taiyo Nissan Co.) from a gas cylinder is ejected through a pulse nozzle (009-0181 900, Parker Hannifin) at an angle of approximately 30° onto the ZnSe plate inside the vacuum chamber, with the pressing pressure regulated at 0.32 MPa using a regulator (NHW-1S-11N1TF). During this process, a pulse nozzle driver (Multi-Channel IOTA ONE, Parker Hannifin) sets the nozzle opening time (On-time) and closing time (Off-time) to 100 ms and 900 ms, respectively.

Subsequently, spectral reference data are acquired through spectroscopic imaging immediately before ejecting the N_2O gas. After N_2O gas ejection, the sample holder temperature is maintained at 100 K for 20 minutes to allow N_2O ice growth, and spectra are obtained.

Next, annealing is performed by varying the temperature between 104 K and 122 K through heating and cooling processes. This temperature control utilizes a temperature controller connected to a 39Ω metal-clad variable resistor at the voltage output terminal inside the vacuum chamber, achieving a $\Delta 1$ K precision.

In a separate process, after growing N_2O ice, a D_2 lamp (manufactured by Mitrika Co.) with wavelengths of 190 nm - 340 nm irradiates the sample at an angle of approximately 30° for several hours at a temperature of 107 K.

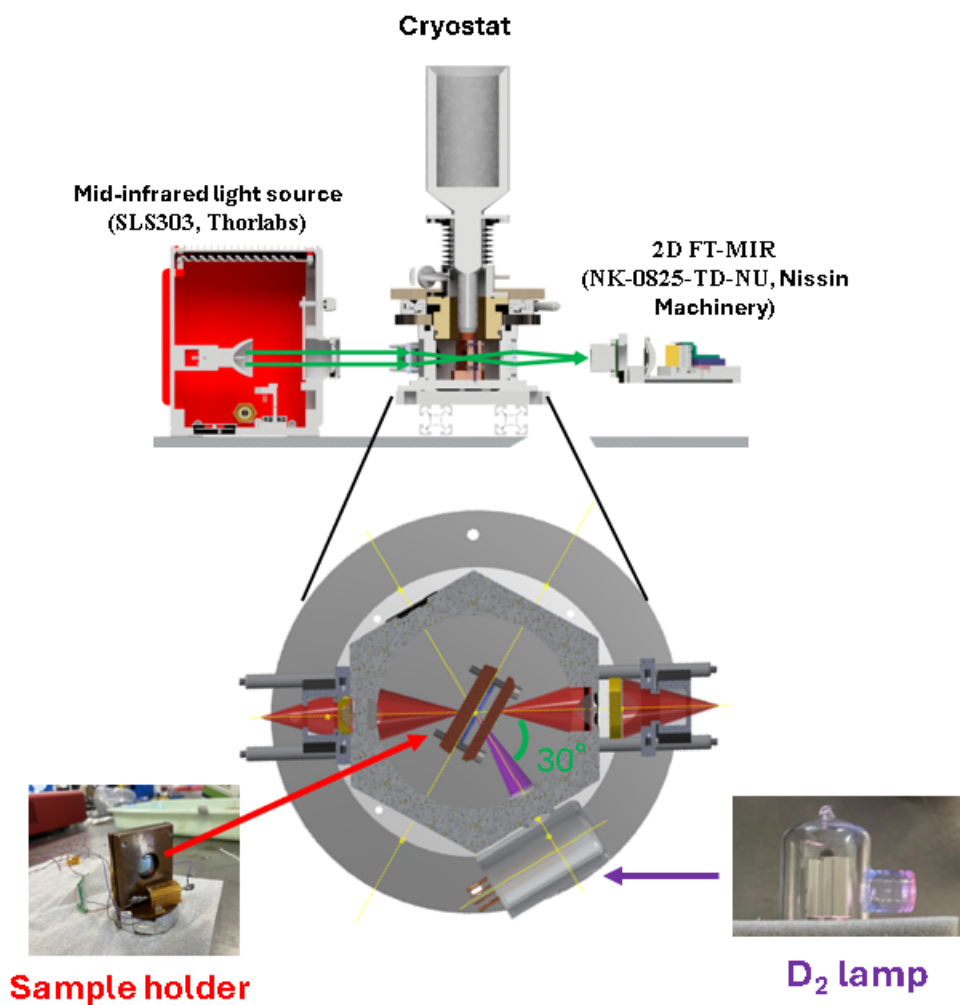


Figure 2: Experimental setup with the mid-infrared light source, vacuum chamber-equipped cryostat, and 2D FT-MIR arranged in a straight line for spectroscopic measurement of N_2O ice growth and alteration processes via mid-infrared transmission absorption imaging spectroscopy. N_2O samples are deposited on a ZnSe plate-equipped sample holder. The distance from the sample holder to the ZnSe lens is set to 52.5 mm, the distance from the ZnSe lens to the multi-slit of the 2D FT-MIR is set to 44.5 mm, and the N_2O sample is observed on the 2D FT-MIR detector at a scale of 1:1. A $39\ \Omega$ metal-clad variable resistor is fixed to the top of the sample holder using aluminum tape using the thermal anchor method. In addition, a D_2 lamp (manufactured by Mitrika Co.) is installed at about 30° to the deposited N_2O ice.

3 Results

3.1 Transmission absorption spectra of N₂O ice and N₂O gas

Figure 3 presents two-dimensional transmission absorption spectra when N₂O gas was ejected with identical pulse parameters into the vacuum chamber under 107 K cooling (red) and at 302.4 K room temperature (blue). The spectra are mapped in 11 × 11 grids, with each grid's spectrum representing an average of a 30 × 30 pixel area, corresponding to 360 × 360 μm on the 2D FT-MIR detector. Each grid's horizontal axis spans 5-15 μm, while the vertical axis represents absorbance from -0.5 to 1.5. Note that the wavelength ranges 5 μm < λ < 7 μm and 14 μm < λ < 15 μm exhibit significant noise as they fall outside the manufacturer's guaranteed range (8 μm < λ < 12 μm). Figure 4 shows an enlarged view of transmission absorption spectra from 4 grids near the center of the N₂O condensed sample.

Under 107 K cooling, several absorption bands are observed: a strong band at 7.75 μm corresponding to the ν₁ vibrational mode (N=O symmetric stretching vibration) of N₂O molecules, a band at 8.60 μm for the 2ν₂ vibrational mode (antisymmetric stretching), a torsion mode at 7.27 μm (Dows 1957), a weak absorption band of the torsion mode at 7.96 μm, and an absorption band of the ν₁+2ν₂ mode at 5.29 μm. All five bands exhibit singlet structures (Table 1). This suggests that N₂O molecules exist in a condensed phase (N₂O ice) due to restricted rotational motion. In contrast, at 302.4 K room temperature, P and R branch doublet structures resulting from vibration-rotation interactions of the ν₁ and 2ν₂ vibrational modes are confirmed, indicating that N₂O molecules exist as gas (N₂O gas). Additionally, the absorption peaks of the ν₁ vibrational mode, 2ν₂ vibrational mode, and torsion mode appear stronger in N₂O ice than in N₂O gas. This suggests that N₂O molecules in the condensed phase, with bond dipole moments of $\frac{\partial \mu}{\partial \mu_{N-N}} = 2.45 \text{ D}/\text{\AA}$ and $\frac{\partial \mu}{\partial \mu_{N-O}} = 5.13 \text{ D}/\text{\AA}$, form a molecular crystal through strong electrostatic interactions due to significant polarization. These polarized N₂O molecules enhance intermolecular interactions via van der Waals forces in the condensed phase.

Table 1: N₂O absorption bands

Chemical species	Wavelength/μm	Vibrational mode
N ₂ O (ice)	7.75	ν ₁
N ₂ O (ice)	8.60	2ν ₂
N ₂ O (ice)	7.27	torsion
N ₂ O (ice)	5.29	ν ₁ +ν ₂
N ₂ O (ice)	7.96	2ν ₂ +91 (torsion)
N ₂ O (gas)	7.70/7.84	ν ₁ (R-branch/P-branch)
N ₂ O (gas)	8.52/8.75	2ν ₂ (R-branch/P-branch)

Table 2: N₂O absorption bands (comparison with previous studies)

Chemical species	Wavelength/μm	Vibrational mode	Reference
N ₂ O (amorphous)	7.79	ν ₁	Mifsud et al. 2022
N ₂ O (crystalline)	7.79	ν ₁	//
¹⁵ N ¹⁴ N ¹⁶ O (crystalline)	7.82	ν ₁	Hudson et al. 2017
¹⁴ N ¹⁴ N ¹⁸ O (crystalline)	7.96	ν ₁	//
N ₂ O (crystalline)	8.58	2ν ₂	//
N ₂ O (crystalline)	5.29	ν ₁ +ν ₂	//
N ₂ O (ice)	7.73	ν ₁	Dows 1957
N ₂ O (ice)	8.57	2ν ₂	//
N ₂ O (ice)	7.22	ν ₁ +92 (torsion)	//
N ₂ O (ice)	5.29	ν ₁ +ν ₂	//
N ₂ O (ice)	7.96	2ν ₂ +91 (torsion)	//

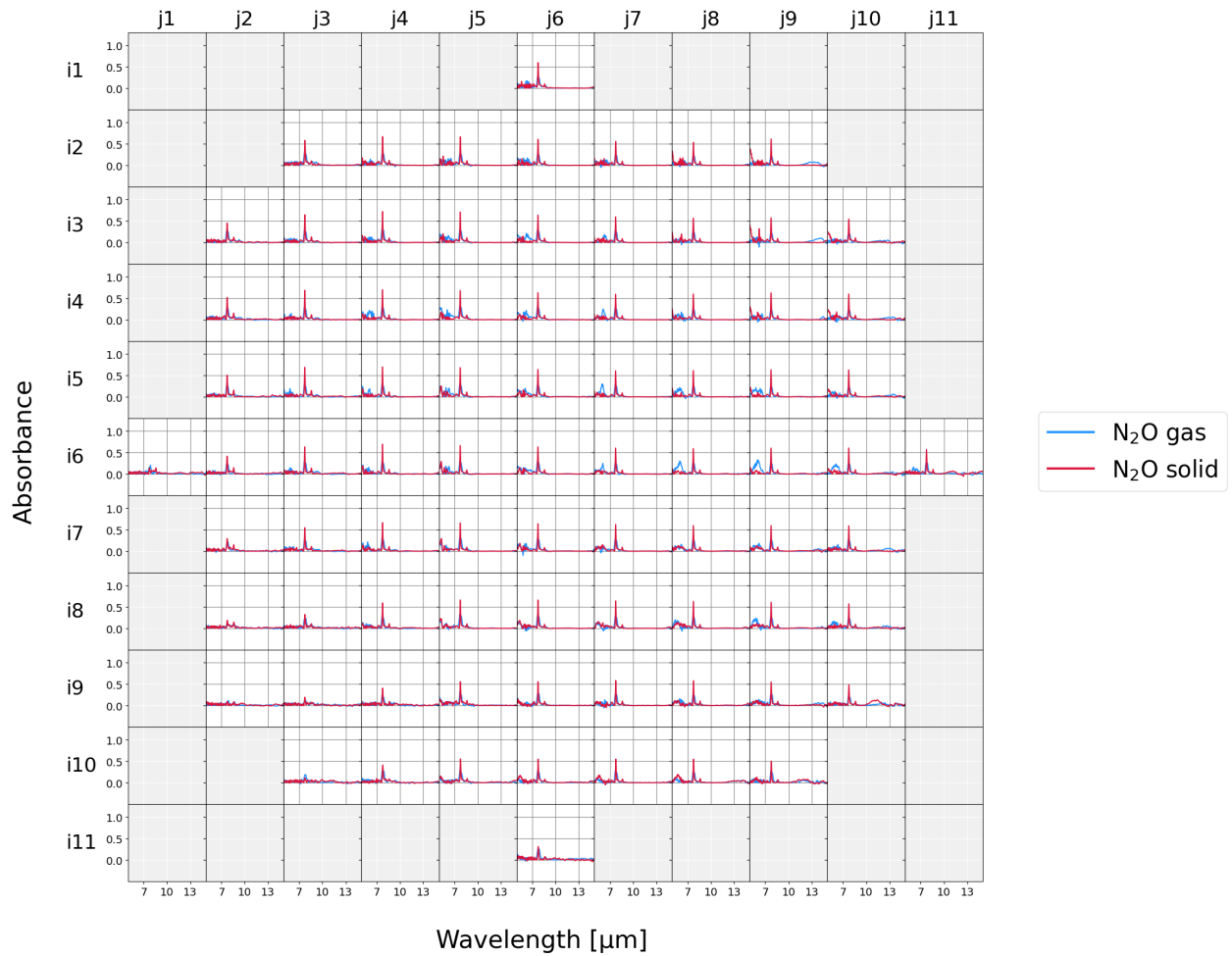


Figure 3: 11×11 grid two-dimensional transmission absorption spectra when identical pulses of N_2O gas were injected into the vacuum chamber under 107 K cooling conditions (red) and at 302.4 K room temperature (blue). The horizontal axis of each grid spans 5-15 μm and the vertical axis represents absorbance from 0.5-1.5.

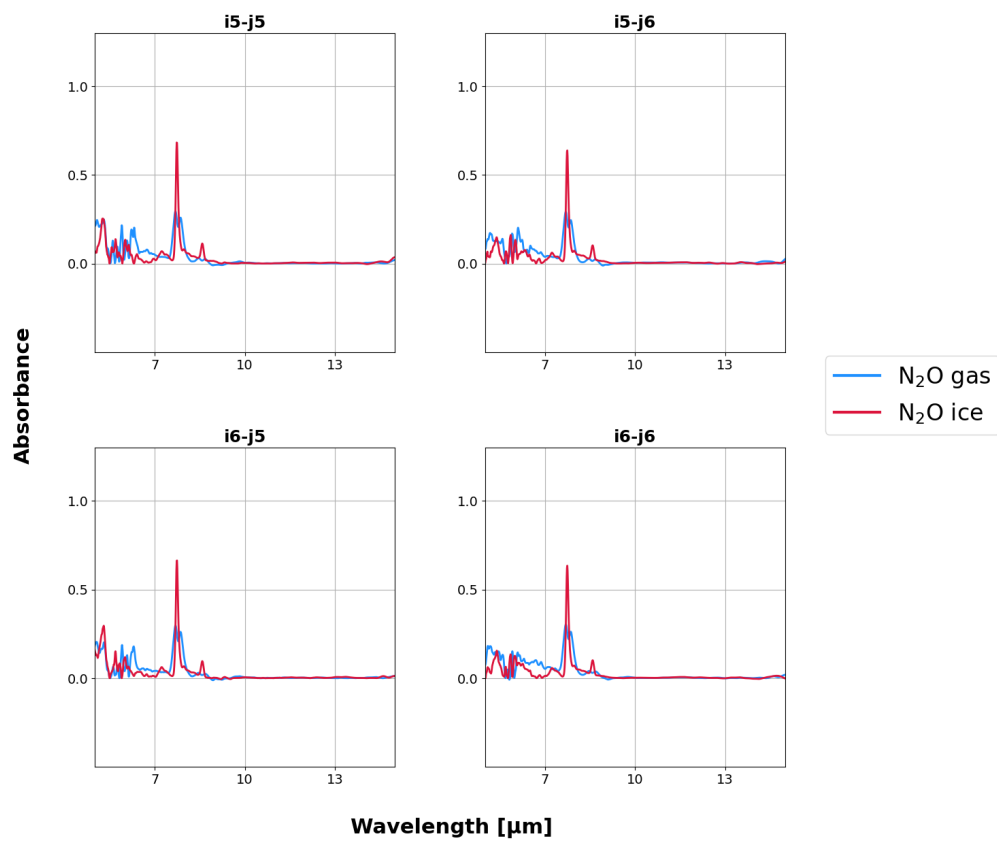


Figure 4: Enlarged transmission absorption spectra of 4 grids near the center of the N₂O condensed sample from Figure 3.

3.2 Annealing of N₂O ice

Figure 5 shows the two-dimensional transmission absorption spectra at 23.5, 31.5, 38.5, 40.6, 45, 49.5, 52.8, and 61.5 minutes after N₂O gas injection. The pressure is 230 Pa, and the temperatures are 110 K, 115 K, 120 K, 122 K, 115 K, 110 K, 107 K, and 104 K. Figure 6 shows the transmission absorption spectra of four grids near the center of the N₂O condensation sample. In all the grids, the torsion (7.27 μm), ν_1 (7.75 μm), and $2\nu_2$ (8.60 μm) vibration modes of N₂O molecules in the condensed phase were enhanced and decreasing the temperature. In addition, we discovered new peaks at around 12 μm and 14 μm . The external factors of temperature rise and fall suggest that a phase transition from the amorphous phase to the crystalline phase is occurring in the solid structure of N₂O ice, that long-range order is being formed between N₂O molecules, and that the density is increasing. In addition, the fact that the absorbance is growing regardless of whether the temperature is rising or falling shows that the crystalline structure changes irreversibly with temperature.

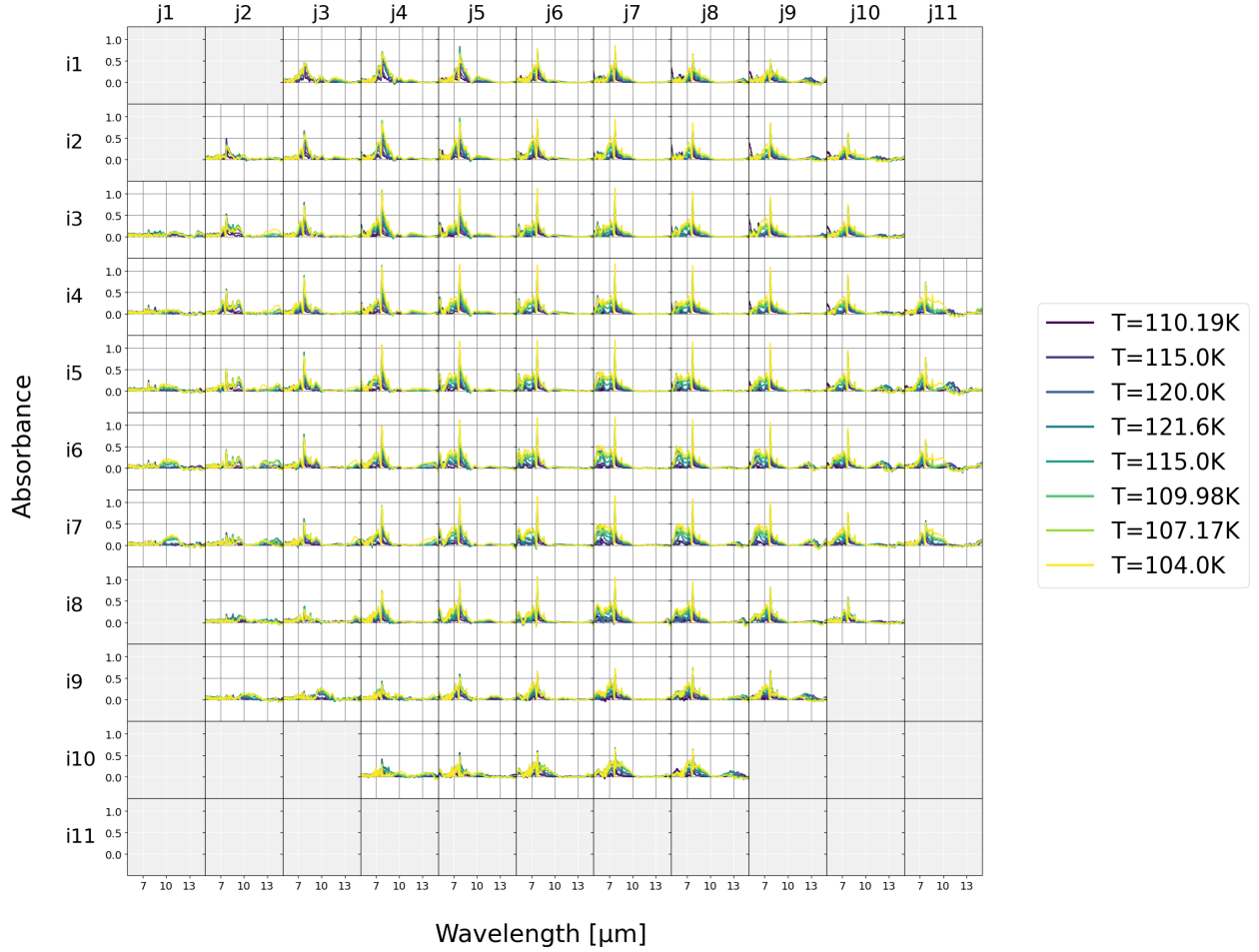


Figure 5: Two-dimensional transmission absorption spectra recorded at temperatures of 110.19 K, 115.0 K, 120.0 K, 121.6 K, 115.0 K, 109.98 K, 107.17 K, and 104.0 K, corresponding to 23.5, 31.5, 38.5, 40.6, 45, 49.5, 52.8, and 61.5 minutes after N₂O gas injection.

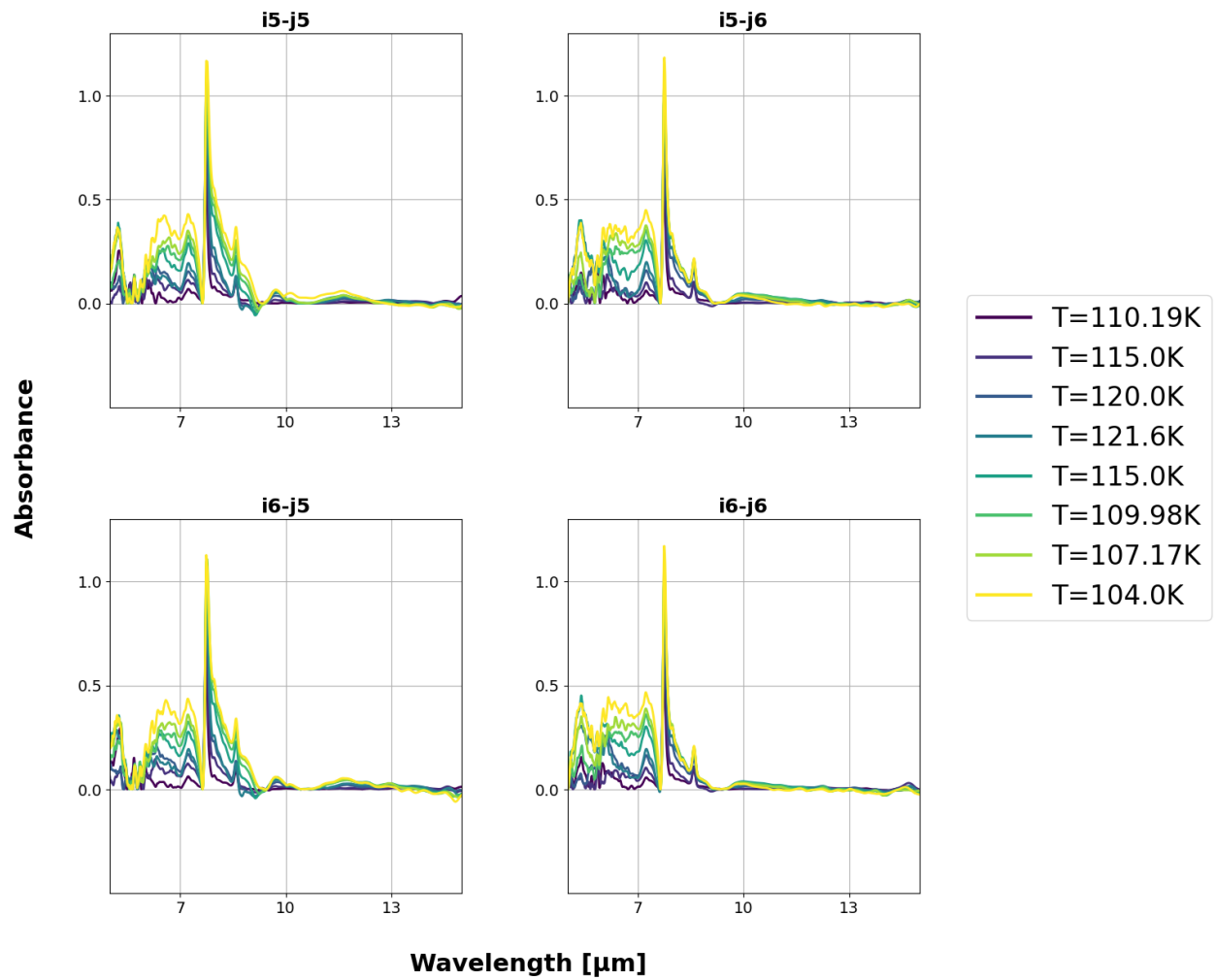


Figure 6: Enlarged two-dimensional transmission absorption spectra of 4 grids near the center of the N_2O condensed sample from Figure 6.

3.3 UV irradiation to N₂O ice

Figure 7 presents two-dimensional transmission absorption difference spectra at 0, 10, 20, 30, 40, 50, 60, 70, 80, 90, 120, 180, 240, 300, 360, 420, and 510 minutes after UV irradiation of N₂O ice under conditions of 41 Pa pressure and 107 K temperature. These difference spectra represent the subtraction of before-UV irradiation spectra from after-UV irradiation spectra. Figure 8 shows an enlarged view of 4 grids near the center of the N₂O condensed sample. Results from HITRAN simulation absorption spectra of N₂O, NO, NO₂, and O₃ under identical temperature and pressure conditions are also presented.

From 20 to 60 minutes of irradiation time, all vibrational modes of N₂O increased. Between 60 and 120 minutes, all N₂O vibrational modes decreased, while absorbance in the 9~10 μm and 11~14 μm wavelength ranges initially increased sharply before decreasing. Notably, between 60 and 80 minutes, vibrational modes of N₂O₃ (ν_4) at 12.73~12.9 μm, NO₂ (ν_2) and N₂O₄ (ν_{12}) at 13.28 μm, and N₂O₅ (ν_{11}) at 12.58 μm increased before subsequently decreasing. After 120 minutes, absorption intensities of various nitrogen oxide ice vibrational modes fluctuated at wavelengths 5.33~5.82 μm, 6.23~6.90 μm, 7.66 μm, 9.59 μm and 10.3 μm, 10.48 μm, and 14.18 μm, corresponding to NO(ν_1), N₂O₄(ν_7/ν_5), cis-(NO)₂, N₂O₃(ν_4) and NO₂(ν_1), N₂O₃, NO₃, and O₃.

These temporal changes in absorbance were confirmed to be reproducible when N₂O ice was irradiated with UV under identical temperature and pressure conditions. Additionally, differences observed between the central and peripheral regions of the condensed sample suggest that the photodissociation process of N₂O ice depends on deposition thickness and crystal structure, indicating complex low-temperature solid-state chemical reactions. Table 3 presents various solid-state vibrational modes confirmed in this study. In contrast, in previous studies, the appendix table from 5 to 7 shows vibrational modes confirmed under multiple conditions.

Table 3: N_xO_y Absorption band (After UV irradiation to N₂O ice at 107 K in condensed phase at temperature 107 K and pressure 41 Pa)

Chemical species	Wavelength/μm	Vibrational mode
NO	5.34	ν_1
N ₂ O ₄	5.33	N=O str
cis-(NO) ₂	5.37	N-O s-str ($a_g(1)$)
N ₂ O ₃	5.45	N=O str
N ₂ O ₂ /cis-(NO) ₂	5.67	N-O a-str ($b_u(5)$)
N ₂ O ₄	5.82	ν_7/ν_5
NO ₂	6.23	N-O a-str
N ₂ O ₃	6.23	N-O a-str
N ₂ O ₃	6.31	ν_2
NO ₃	6.90	-
N ₂ O ₃	7.66	ν_3
NO ₂	7.66	ν_1
O ₃	9.59	ν_3 O-O a-str
O ₃	10.3	O-O a-str
NO ₃	10.48	ν_1
NO ₃	12.40	-
N ₂ O ₃	12.73	ν_4
N ₂ O ₃	12.90	NO ₂ deform
NO ₂ /N ₂ O ₄	13.28	ν_2/ν_{12}
N ₂ O ₅	13.58	ν_{11}
O ₃	14.18	-

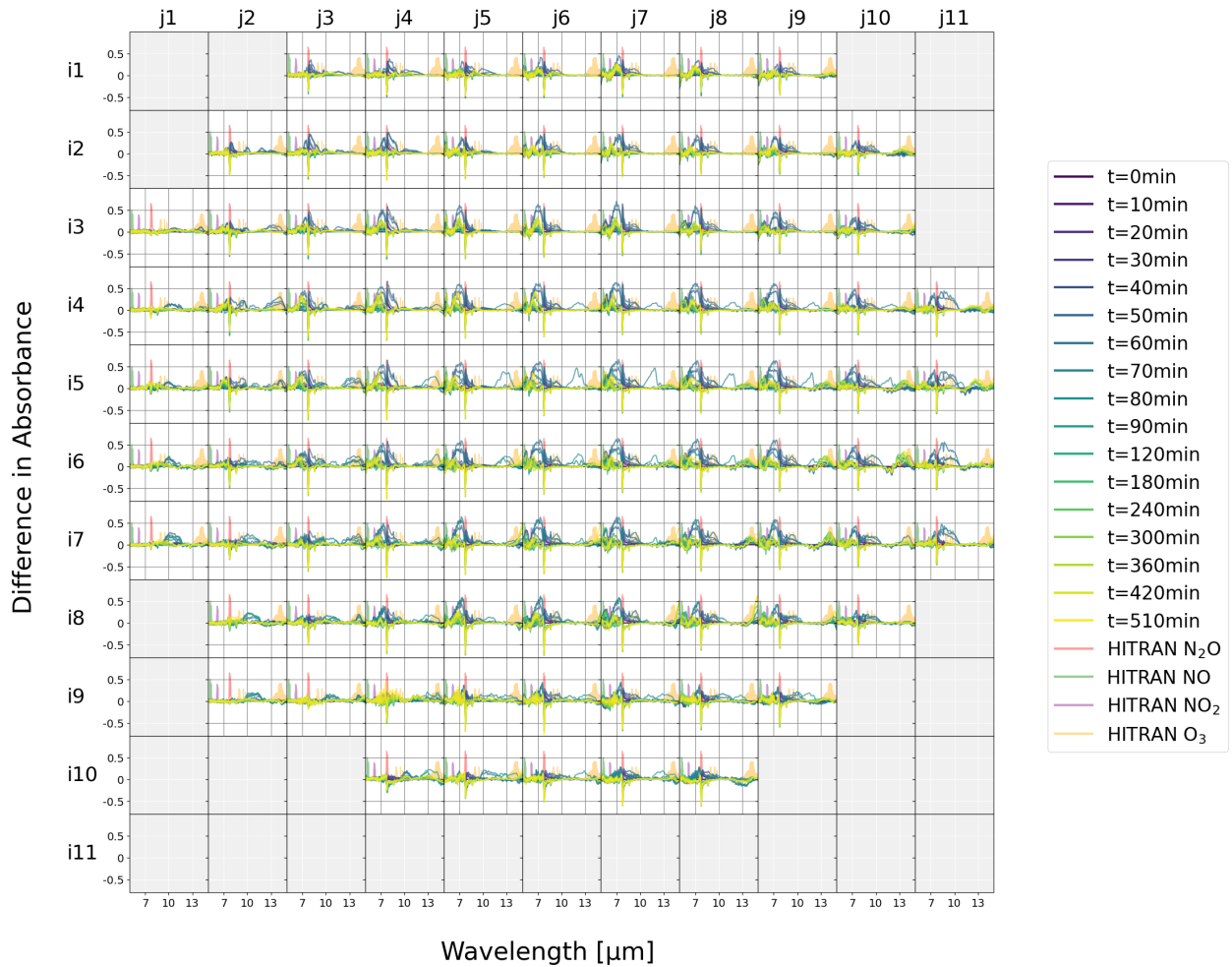


Figure 7: Two-dimensional transmission absorption difference spectra of N₂O ice under UV irradiation at a constant temperature of 107 K, measured at 0, 10, 20, 30, 40, 50, 60, 70, 80, 90, 120, 180, 240, 300, 360, 420, and 510 minutes after initial exposure. HITRAN gas simulations for N₂O, NO, NO₂, and O₃ are also shown.

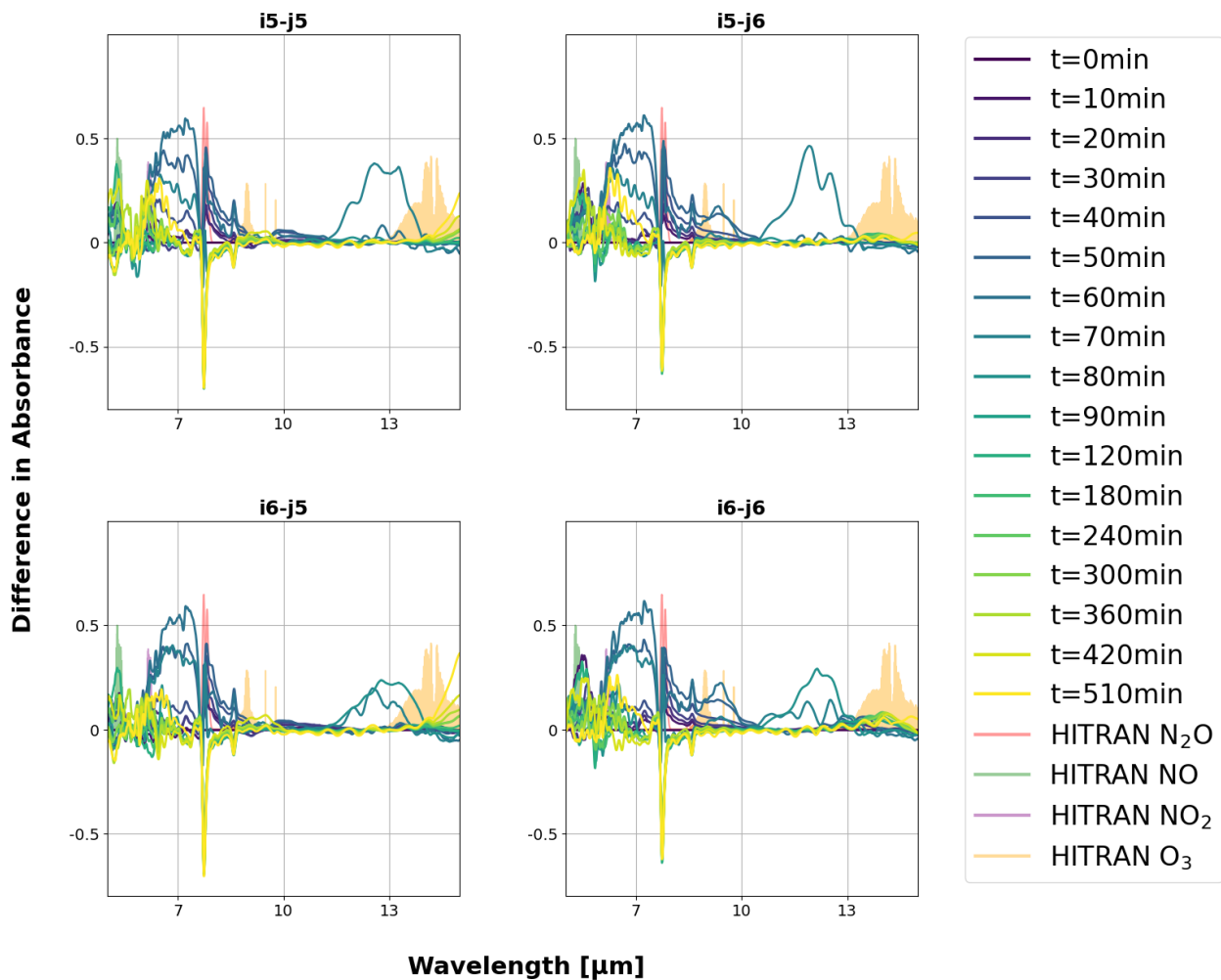


Figure 8: Enlarged two-dimensional transmission absorption difference spectra of 4 grids near the center of the N₂O condensed sample from Figure 8.

4 Discussion

4.1 Crystal structure and intermolecular distance of N₂O molecules in the condensed phase

N₂O crystallizes in a cubic system with Pa3 space group at temperatures below 182.35 K, containing four N₂O molecules per unit cell (Figure 9) (Kuchta and Etters 1992). The N-N bond distance measures 1.145 Å, the N-O bond distance is 1.120 Å, and the permanent dipole moment equals $\mu = 0.17$ D (Wang et al. 2001). However, since the intermolecular distances in solid-phase N₂O ice remain undetermined, we estimate these distances from the absorbance values of N₂O ice obtained in our experiment. For this estimation, we assume that all unit cells of the deposited N₂O ice exhibit a cubic crystal structure and form continuous arrangements.

The Lambert-Beer law applies since we observe infrared light that has undergone multiple reflections by particles within the N₂O ice (Equation 2).

$$A = \varepsilon cl \quad (2)$$

Define as absorbance $A = 0.7224$, ε represents the absorption coefficient at 70 K which equals 9.747×10^{-16} m/molecule (Hudson et al. 2017), c denote the column density in molecule/cm² and l indicate the optical path length in meters, which corresponds to the N₂O ice thickness. Assuming the ideal gas equation of state, the thickness of N₂O ice l in meters can be expressed by equation (3) from equation (2).

$$l = \left[\sum_i^n \frac{(P_{\text{after}} - P_{\text{before}})V_{\text{chamber}}}{RT_i} \right] \frac{V_{\text{chamber}}}{S_{\text{sh}}\rho_{\text{crystalline}}} \quad (3)$$

S_{sh} represents the sample holder surface area of 6.907×10^{-3} m², and $\rho_{\text{crystalline}}$ denotes the density of crystalline N₂O ice at 70 K, which equals 1.591×10^3 kg/m³ (Hudson et al. 2017). V_{chamber} indicates the vacuum chamber volume of 2.623×10^{-4} m³, R is the gas constant 8.314 J/K mol, T_i represents the temperature in K at each time when N₂O gas was ejected through the pulse nozzle, P_{after} denotes the pressure in Pa inside the vacuum chamber after each N₂O gas ejection, and P_{before} indicates the pressure in Pa inside the vacuum chamber before each N₂O gas ejection.

The thickness of the N₂O ice layer, calculated from Equation (3), is $l = 1.1 \times 10^{-7}$ m, and the column density c is 6.7×10^{21} molecules/m². The number of N₂O ice molecules per unit volume, calculated by dividing the column density by the thickness, equals 6.1×10^{28} molecule/m³. The N₂O ice volume, obtained by multiplying the thickness by the sample holder area, equals 7.6×10^{-10} m³. Therefore, the total number of molecules in the deposited N₂O ice, calculated by multiplying the number of molecules per unit volume by the N₂O ice volume, equals 4.7×10^{19} molecules.

Since each unit cell contains four N₂O molecules, the number of lattices k equals 1.2×10^{19} . Consequently, the volume per unit cell, calculated by dividing the N₂O ice volume by the number of lattices, equals 6.5×10^{-29} m³/molecule. From these calculations, assuming that the length of each side of the cubic crystal system is the same, the intermolecular distance of N₂O molecules in the condensed phase is given by Equation (4). Therefore, we estimate that the intermolecular distance of N₂O in the condensed phase is approximately 3.5 times the interatomic bond distance.

$$(6.53 \times 10^{-29})^{\frac{1}{3}} = 4.03\text{\AA} \quad (4)$$

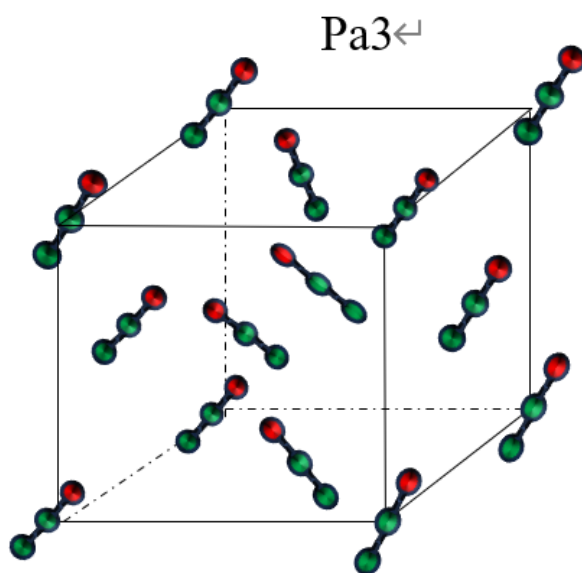


Figure 9: Crystal structure of N₂O molecules in the condensed phase. The structure is cubic with Pa $\bar{3}$ space group, containing 4 N₂O molecules per unit cell (Kuchta and Etters 1992). Red represents nitrogen atoms, and green represents oxygen atoms.

4.2 Spectral evolution of N₂O ice following thermal annealing

Figure 10 illustrates changes in column density relative to temperature variations for N₂O ice vibrational modes: torsion (7.27 μm), ν₁ (7.75 μm), 2ν₂ (8.60 μm), 12 μm, and 14 μm. In each 11 × 11 grid, the horizontal axis represents temperature in K, while the vertical axis indicates column density in molecules/cm² calculated using equations (2) and (3). Arrows within each grid correspond to the sequence of temperature changes.

All vibrational modes exhibit irreversible rate increases with temperature. During the temperature rise period (110.19 K → 121.6 K), the rate of absorbance increase is substantial, whereas during the temperature decrease period (121.6 K → 104.0 K), this rate is smaller. This suggests that crystallization progresses rapidly during temperature rise as intermolecular distances between N₂O molecules contract and density increases, while crystallization advances more slowly during temperature decrease. Additionally, near the center of the condensed sample, the increase rates at 12 μm and 14 μm are smaller but larger at the periphery. This suggests that thinner deposition regions exhibit greater increase rates at 12 μm and 14 μm.

Figure 11 depicts the rate of column density change R %/K with temperature for torsion (7.27 μm), ν₁ (7.75 μm), 2ν₂ (8.60 μm), 12 μm, and 14 μm vibrational modes. The relative change rate R %/K with temperature is calculated using equation 5:

$$R = \frac{N_i - N_0}{N_0} \times 100 \quad (5)$$

For the heating phase ($T_0 = 110.19$ K → $T_1 = 121.6$ K), we utilized column density values N_0 at 110.19 K and N_i at 121.6 K. Conversely, for the cooling phase ($T_0 = 121.6$ K → $T_1 = 104.0$ K), we employed column density values N_0 at 121.6 K and N_i at 104.0 K. Figure 11 reveals that during heating, all vibrational modes demonstrate large positive change rates. Notably, torsion and 2ν₂ modes exhibit particularly high positive rates near the center of the condensed sample, indicating faster crystallization in thicker deposition regions. In contrast, outer areas frequently show negative rates, suggesting possible sublimation in thinner deposition regions during heating. These findings demonstrate that N₂O ice undergoes irreversible temperature-dependent crystallization exclusively in thicker deposition regions.

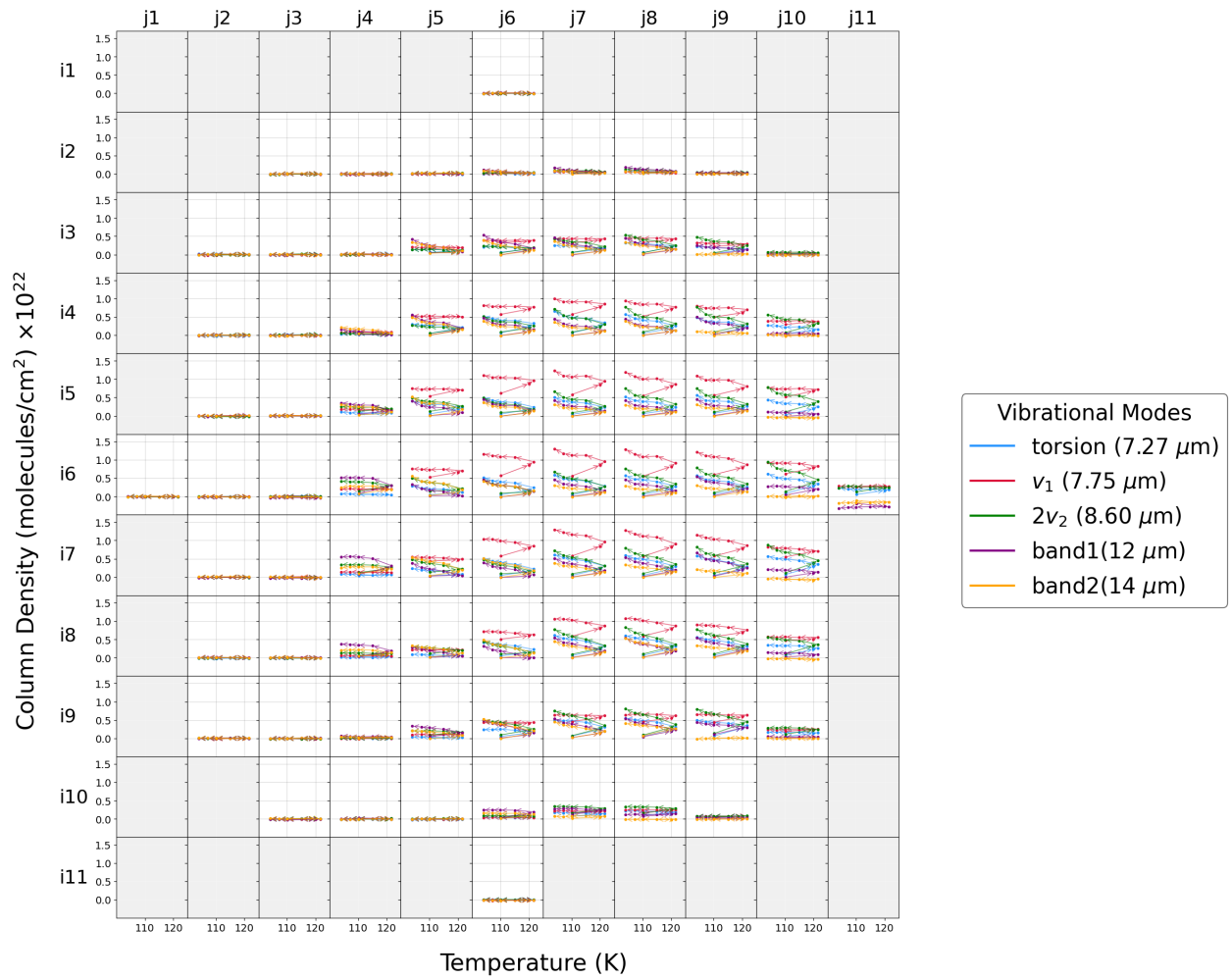


Figure 10: Changes in column density of N₂O ice as a function of temperature. The horizontal axis represents temperature in K, while the vertical axis shows column density in molecules/cm² calculated from equations (2) and (3). Arrows correspond to the sequence of temperature variations.

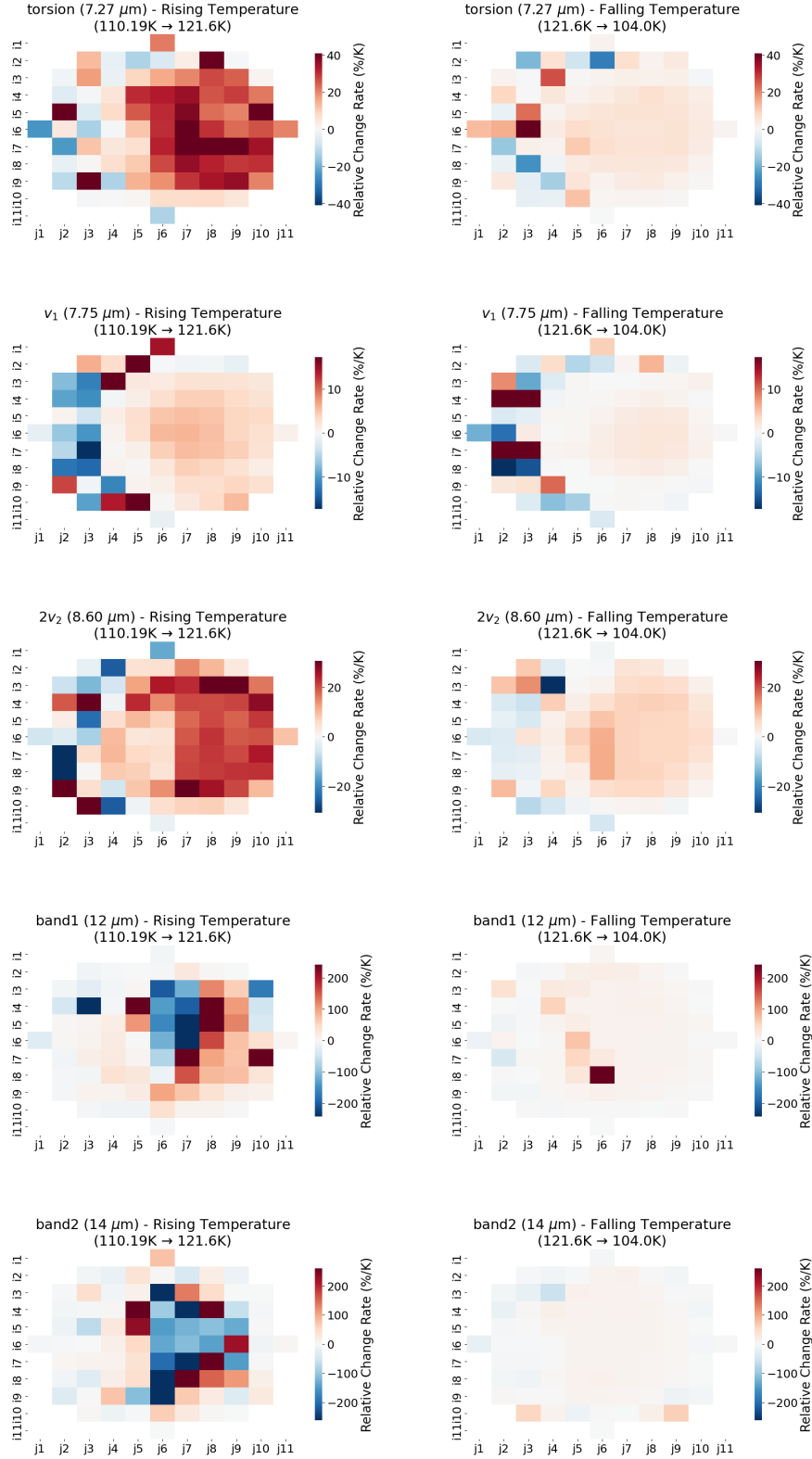


Figure 11: The rate of change in column density for temperature (%/K) for the torsion ($7.27 \mu\text{m}$), ν_1 ($7.75 \mu\text{m}$), $2\nu_2$ ($8.60 \mu\text{m}$), $12 \mu\text{m}$, and $14 \mu\text{m}$ vibrational modes during temperature increase ($110.19 \text{ K} \rightarrow 121.6 \text{ K}$) and temperature decrease ($121.6 \text{ K} \rightarrow 110.19 \text{ K}$), as determined by equation (5).

4.3 Solid surface chemical reactions of N₂O ice by UV irradiation

Figure 12 presents a two-dimensional representation of temporal changes in peak absorbance for each vibrational mode listed in Table 3, displayed as 11×11 grids. The horizontal axis represents UV irradiation time from 0 to 510 min, while the vertical axis indicates column density in molecules/cm². Experimental data points are fitted using linear interpolation. After UV irradiation, the column density of the ν_1 vibration mode of N₂O molecules in the condensed phase at a wavelength of 7.75 μm decreases rapidly between 60 and 90 min, suggesting that N₂O is photodissociated. Since the dissociation limits of the N-O bond and N-N bond are 741.5 nm and 251.5 nm, respectively, we can assume that these bonds were broken by UV irradiation in the wavelength range of 190 nm to 340 nm. The fact that electrons in N₂O molecules transition from the ground state to the excited state and that charge transfer occurs between N₂O molecules suggests that a chemical reaction occurs on the surface of the solid. As a result, the formation and dissociation of various nitrogen oxide ices such as N₂O₃ (m.p. 173 K), NO₂ (m.p. 262 K), N₂O₄ (m.p. 295 K), N₂O₅ (m.p. 308 K), NO (m.p. 109.5 K), and other nitrogen oxide ice formation and dissociation occurred.

We estimate the two-dimensional rate constant k /s for a pseudo-first-order reaction represented by equation (6). We define the formation rate as k /s and the dissociation rate as $-k$ /s, with $[A]$ and $[B]$ representing reactant column densities in molecules/cm² and $[C]$ denoting product column density in molecules/cm².



Under this assumption, Figure 12 displays color maps of the normalized rate $|k|$, calculated by dividing the rate of change in column density $[N]$ molecules/cm² by the column density itself, as expressed in equation (7). Figure 13 illustrates the formation rate, dissociation rate, and their difference.

$$|k| = \frac{d[N]}{dt} \cdot \frac{1}{[N]} \quad (7)$$

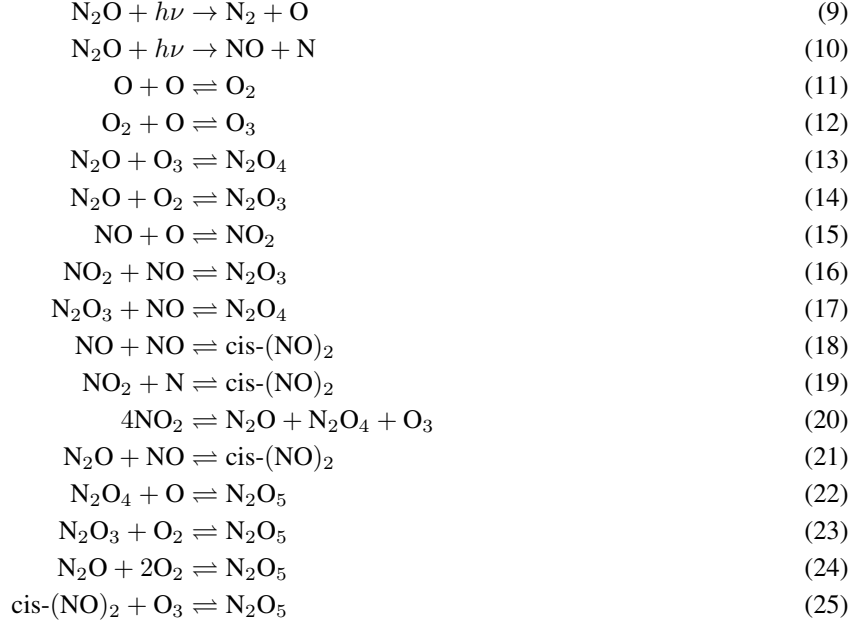
The analysis includes various molecular vibrational modes: NO molecules at 5.34 μm (ν_1 mode), cis-(NO)₂ at 5.67 μm , NO₂ at 6.23 μm (ν_1 mode), N₂O at 7.75 μm (ν_1 mode), O₃ at 14.18 μm , N₂O₄ at 13.28 μm (ν_7/ν_5 modes), N₂O₃ at 7.66 μm (ν_4 mode), NO₃ at 6.90 μm , and N₂O₅ at 13.58 μm .

Notably, the N₂O molecules at 7.75 μm (ν_1 mode) exhibit a high dissociation rate ($|k| \sim 7 \times 10^{-2}$ /s) near the condensed sample center, while showing elevated formation rates ($|k| \sim 3 \times 10^{-3}$ /s) in peripheral regions. We also calculated the D₂ lamp photon flux ϕ_{D_2} using equation (8), where P represents the irradiation power $P = 6009 \text{ W/m}^2$, t the irradiation time, h Planck's constant, c the speed of light, and A the sample holder area.

$$\phi_{D_2} = \int_{190 \text{ nm}}^{340 \text{ nm}} \frac{Pt\lambda}{hcA} d\lambda \quad (8)$$

The two-dimensional pattern of N₂O molecules at 7.75 μm (ν_1 mode) suggests that dissociation reactions are dominant in regions with high D₂ lamp irradiation intensity ($\phi_{D_2} \sim 10^{23}$ photons/m²). On the other hand, formation reactions are dominant in regions with low irradiation intensity. For comparison, the formation constant of N₂O ice when irradiating a mixture of N₂ and CO ice with 10 keV electrons at 10 K was estimated at 6.4×10^{-2} /s (Jamieson et al. 2005).

Figure 14 illustrates the chemical reaction network initiated by N₂O ice photodissociation, as observed through changes in transmission absorption spectra following UV irradiation. When external UV energy irradiates N₂O ice, N-N and N-O bonds break, transforming into N₂ or NO within 60-90 minutes (equations 9, 10). Simultaneously, charge transfer occurs at the solid surface, forming oxygen atoms, oxygen molecules, and ozone (equations 11, 12), while N₂O₃ and N₂O₄ undergo rapid formation and dissociation between 60-80 minutes (equations 13, 14). From 90-180 minutes, oxygen atoms mediate repeated formation and dissociation of NO and NO₂ (equation 15), followed by N₂O₃ and N₂O₄ cycling through NO and NO₂ intermediates between 180-400 minutes (equations 16, 17). Between 400-510 minutes, cis-(NO)₂ forms and dissociates via NO, NO₂, and nitrogen atom intermediates (equations 18, 19). Additionally, N₂O regenerates from NO₂ dissociation (equation 20), subsequently participating in cis-(NO)₂ cycling through NO intermediates (equation 21). Ultimately, N₂O₅ undergoes formation and dissociation cycles from N₂O₃, N₂O₄, N₂O, and cis-(NO)₂ precursors, mediated by oxygen atoms, molecules, and ozone (equations 22-25). This complex N_xO_y solid-state chemical reaction network, initiated by N₂O ice photodissociation, exhibits time and deposition thickness dependencies. These findings suggest that N₂O ice formed from N₂ and CO ices on Pluto's and Triton's surfaces and atmospheres likely experiences similar complex N_xO_y species formation and dissociation processes upon UV exposure.



In the future, we will attempt to quantitatively predict the N_xO_y species in the atmosphere by determining the dissociation and formation constants, reaction barriers, and activation energies, taking into account the temperature dependence, by irradiating N_2O ice with UV light of intensity ($\phi_{\text{D}_2} \sim 10^{16}$ photons/m²) that simulates the actual atmospheric environment under various temperature conditions. Additionally, we aim to conduct UV irradiation of solid mixtures, including N_2 ice and CO ice, and to observe vibrational modes of N_xO_y species in the unexplored near-infrared wavelength bands of 2-5 μm and 15-20 μm using newly developed 2D-FTIR (Table 4) (Zhao et al. 2024). It is possible to compare it with future observations that will be carried out in the 2040s and 2060s, such as the "Arcanum mission" (McKevitt et al. 2024) and "2044: A DEEP Space Odyssey" (May et al. 2025).

Table 4: Vibration modes of N_xO_y species in the near-infrared wavelength range that we aim to observe in the future

Species	Wavelength/ μm	Vibrational mode	Reference
N_2O (amorphous)	4.47	ν_3	Hudson et al. 2017
N_2O (crystalline)	17.0	ν_2	//
N_2O (crystalline)	2.85	$\nu_1 + \nu_3$	//
N_2O (crystalline)	2.96	$2\nu_2 + \nu_3$	//
N_2O (solid)	3.55	$\nu_2 + \nu_3$	//
N_2O (solid)	3.88	$2\nu_1$	//
N_2O (solid)	4.05	$\nu_1 + 2\nu_2$	//
N_2O_4 (crystalline)	3.27	$\nu_1 + \nu_9$	Fulvio et al. 2019
N_2O_4 (crystalline)	2.91	$\nu_5 + \nu_9$	//
cis-(NO) ₂ (solid)	2.77	tentative	Bergantini et al. 2022b
NO ₂ (solid)	3.44	$\nu_1 + \nu_3$	//

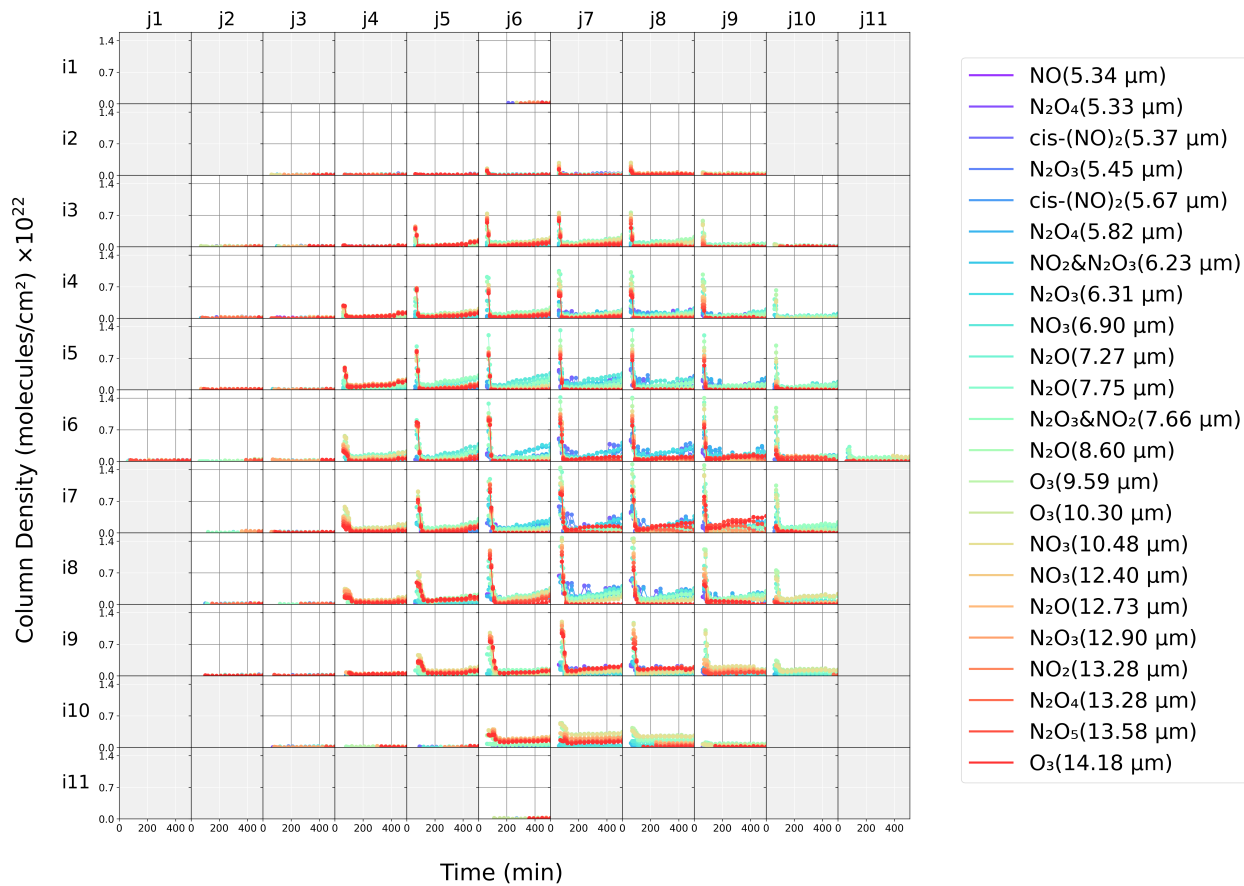


Figure 12: Column density evolution of N_xO_y species originating from N_2O ice photodissociation as a function of time. The horizontal axis represents UV irradiation time from 0 to 510 min, while the vertical axis shows column density in molecules/cm² calculated from equations (2) and (3).

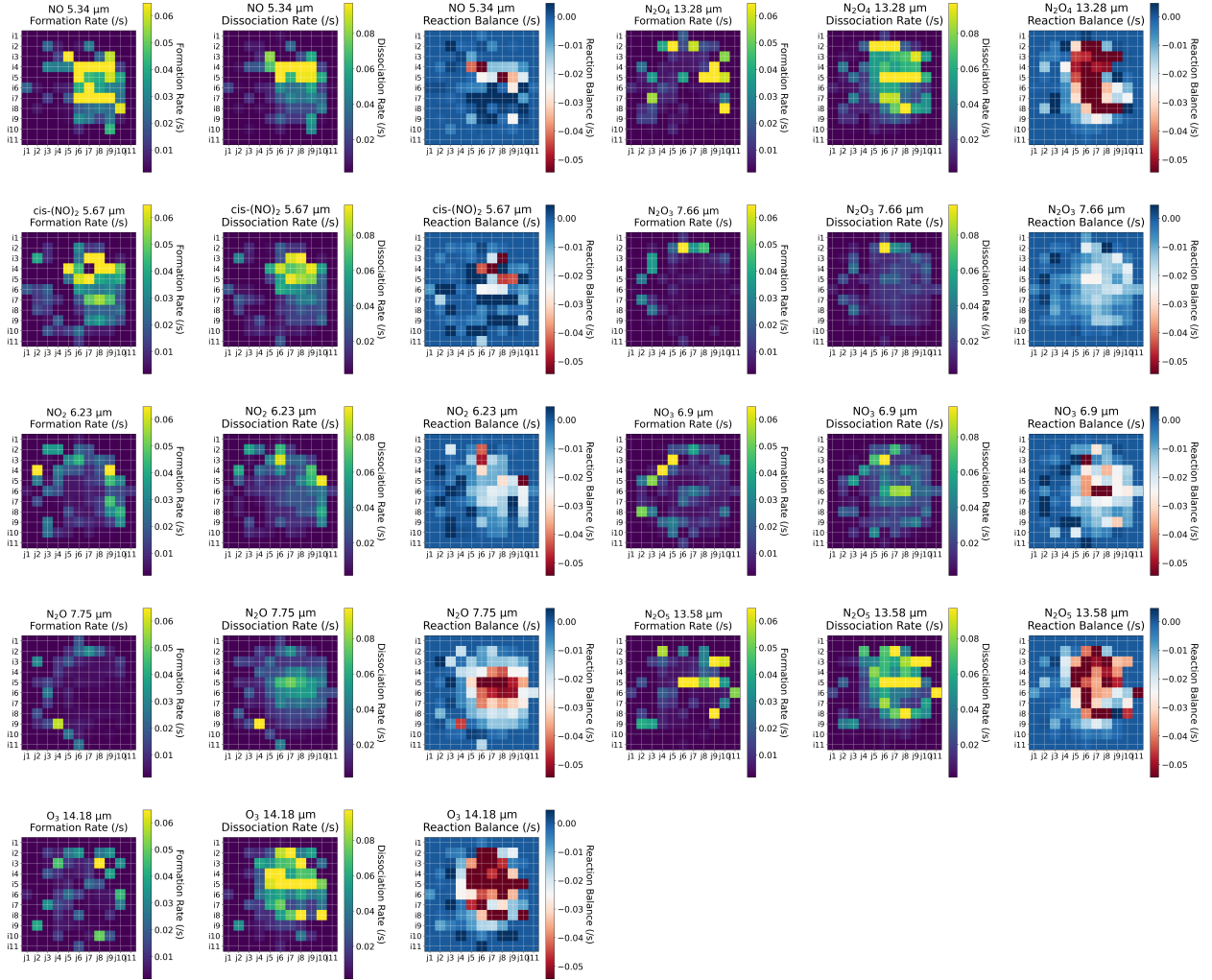


Figure 13: Two-dimensional color map of the normalized rate of change /s calculated by dividing the rate of change in column density for each molecular species, as defined in equation (7).

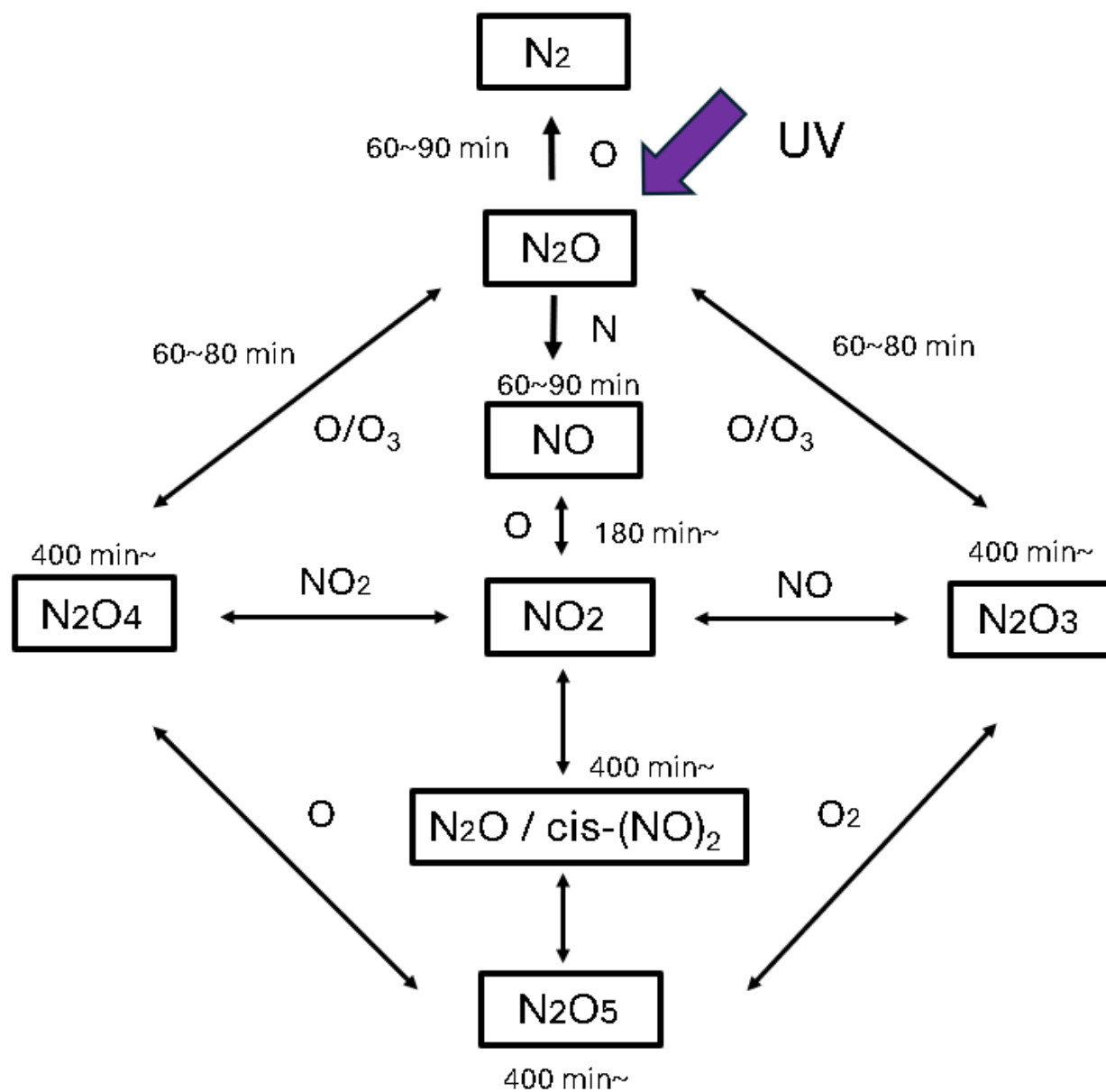


Figure 14: Chemical reaction network of N_xO_y ices initiated by photodissociation of N_2O ice at 107 K temperature.

5 Summary

We simulated the atmospheric environment of outer solar system bodies such as Pluto and Triton (100 K, 10^{-2} Pa) and acquired two-dimensional mid-infrared transmission absorption spectra of N_2O gas condensates.

Spectroscopic imaging revealed a strong absorption band at $7.75 \mu\text{m}$ (N_2O molecule ν_1 vibrational mode), as well as weak absorption bands at $8.60 \mu\text{m}$ (N_2O $2\nu_2$), $7.27 \mu\text{m}$ (N_2O torsion), and $5.29 \mu\text{m}$ (N_2O $\nu_1+\nu_2$). The absorption peaks of the ν_1 vibrational mode, $2\nu_2$ vibrational mode, and torsion mode were stronger than those in N_2O gas. This suggests that the molecular crystal exhibits strong electrostatic interactions due to significant polarization, and polarized N_2O molecules enhance intermolecular interactions via van der Waals forces in the condensed phase.

Additionally, we simulated high-temperature regions of 90 K - 110 K by performing annealing ($110.19 \text{ K} \rightarrow 121.6 \text{ K} \rightarrow 104.0 \text{ K}$). As a result, all vibrational modes of N_2O molecules increased irreversibly with temperature. During the temperature rise period ($110.19 \text{ K} \rightarrow 121.6 \text{ K}$), the rate of absorbance increase was substantial, whereas during the temperature decrease period ($121.6 \text{ K} \rightarrow 104.0 \text{ K}$), this rate was smaller. This suggests that crystallization progresses rapidly during temperature rise and more slowly during temperature decrease.

Subsequently, to reproduce photodissociation reactions, we conducted 8.5 hours of ultraviolet irradiation (190 nm-340 nm) using a D_2 lamp. Following UV irradiation, all vibrational modes of N_2O decreased between 60 and 90 minutes. This likely resulted from breaking N-N bonds (dissociation limit 251.5 nm) and N-O bonds (dissociation limit 741.5 nm) in N_2O ice, transforming into N_2 or NO. Between 60 and 80 minutes, vibrational modes increased at wavelengths $12.73\sim 12.9 \mu\text{m}$ for N_2O_3 (ν_4), $13.28 \mu\text{m}$ for NO_2 (ν_2) and N_2O_4 (ν_{12}), and $12.58 \mu\text{m}$ for N_2O_5 (ν_{11}). After 120 minutes, absorption intensities of various nitrogen oxide ice vibrational modes fluctuated at wavelengths $5.33\sim 5.82 \mu\text{m}$, $6.23\sim 6.90 \mu\text{m}$, $7.66 \mu\text{m}$, $9.59 \mu\text{m}$ and $10.3 \mu\text{m}$, $10.48 \mu\text{m}$, and $14.18 \mu\text{m}$, corresponding to $\text{NO}(\nu_1)$, $\text{N}_2\text{O}_4(\nu_7/\nu_5)$, $\text{cis}(\text{NO})_2$, $\text{N}_2\text{O}_3(\nu_4)$ and $\text{NO}_2(\nu_1)$, N_2O_3 , NO_3 , and O_3 . This suggests that UV photons ($\sim 10^{23}$ photons/ m^2) caused electrons in N_2O molecules to transition from ground to excited states, generating charge transfer between N_2O molecules and triggering solid-surface chemical reactions. Consequently, through the movement of intermediates such as O and species like O_2 , NO, and NO_2 , various nitrogen oxides including N_2O_3 (m.p. 173 K), NO_2 (m.p. 262 K), N_2O_4 (m.p. 295 K), N_2O_5 (m.p. 308 K), and NO (m.p. 109.5 K) repeatedly formed and dissociated.

Based on the decrease and formation rates of peak absorbance for vibrational modes of each molecular species, we estimated pseudo-first-order reaction rates $/s$ in two dimensions. Results showed that dissociation reactions ($7 \times 10^{-3} /s$) proceeded near the center of the condensed sample, while formation reactions ($3 \times 10^{-3} /s$) occurred near the periphery. Therefore, the photodissociation process of N_2O ice clearly depends on UV irradiation intensity. This study reveals for the first time that the low-temperature solid-state chemical network of N_xO_y species, initiated by photodissociation of N_2O ice through UV irradiation, repeatedly undergoes complex dissociation and formation processes depending on time and deposition thickness ($\sim 1 \mu\text{m}$).

Abbreviations

IR	Infrared
2D FT-MIR	Imaging Fourier transform mid-infrared spectrometer
ALMA	The Atacama Large Millimeter/submillimeter Array
UV	ultraviolet
DEEP	Discovering Extra-Neptunian and Extrasolar Phenomena

Declarations

Availability of data and materials

Raw data were generated at the Department of Earth and Planetary Sciences, Graduate School of Environmental Studies, Nagoya University. Derived data supporting the findings of this study are available from the corresponding author DT and co-authors RK and YH on request. The 2D transmission absorption spectrum creation and FFT transformation codes we developed are available on GitHub (<https://github.com/daikitakama>). The specifications for the 2D-FTMIR (NK-0812-TD-NU) can be obtained from the Nisshin Machinery Co. site (<https://nissin-kikai.co.jp/company/>). The intensity spectrum of the D₂ lamp (A5211TH) used during UV irradiation can also be obtained from the Mitrica Co. site (https://www.milas.co.jp/product_d2.html).

Competing interests

The authors declare that they have no competing interests.

Funding

This work was supported by JSPS KAKENHI Grant Numbers JP21J00734, JP22K14084, JP20KK0074, JP19H01950, JP21K18640. This work was carried out by the joint research program of the Institute for Space–Earth Environmental Research, Nagoya University.

Authors' contributions

DT summarized the data and wrote the manuscript with RK, SN, and YH contributions. FI contributed to writing the manuscript and supported the experiment. BZ and YL set up the instruments and supported the experiment. RK also developed the FFT data analysis method.

Acknowledgments

The authors thank the Nagoya University Instrument Development Center for creating the vacuum chamber and repairing the dewar bottle.

Authors' information

¹Graduate University for Advanced Studies/Japan Aerospace Exploration Agency (JAXA)/Institute of Space and Astronautical Science (ISAS), Sagami-hara, Kanagawa 252-5210, Japan.

²Graduate School of Data Science, Nagoya City University, Nagoya, Aichi 467-8601, Japan.

³Graduate School of Environmental Studies, Nagoya University, Nagoya, Aichi 464-8601, Japan.

⁴National Institute of Advanced Industrial Science and Technology (AIST), Onogawa 16-1, Tsukuba, Ibaraki 305-8569, Japan.

References

- Bergantini A, et al. (2022a) On the synthesis of N–O bearing species in astrophysical ices – an infrared spectroscopic study using heavy-ion irradiation of solid N₂:CO samples. *Mon Not R Astron Soc* 511:31–41. <https://doi.org/10.1093/mnras/stab3685>
- Boduch P, Dartois E, Barros A, da Silveira E, Domaracka A, Lv X, Palumbo ME, Pilling S, Rothard H, Duarte E, Strazzulla G (2015) Radiation effects in astrophysical ices. *J Phys: Conf Ser* 629:012008. <https://doi.org/10.1088/1742-6596/629/1/012008>
- Allodi MA, Baragiola RA, Baratta GA, Barucci MA, Blake GA, Boduch P, Brucato JR, Contreras C, Cuyllé SH, Fulvio D, Gudipati MS, Ioppolo S, Kaňuchová Z, Lignell A, Linnartz H, Palumbo ME, Raut U, Rothard H, Salama F, Savchenko EV, Sciamma-O’Brien E, Strazzulla G (2013) Complementary and emerging techniques for astrophysical ices processed in the laboratory. *Space Sci Rev* 180:101–175. <https://doi.org/10.1007/s11214-013-0020-8>
- Grundy WM, et al. (2016) Surface compositions across Pluto and Charon. *Science* 351(6279):aad9189. <https://doi.org/10.1126/science.aad9189>
- Schenk PM, et al. (2021) Triton: Topography and geology of a probable ocean world with comparison to Pluto and Charon. *Remote Sens* 13(3476). <https://doi.org/10.3390/rs13173476>
- Singer KN, et al. (2022) Large-scale cryovolcanic resurfacing on Pluto. *Nat Commun* 13(1542). <https://doi.org/10.1038/s41467-022-29056-3>
- Jamieson CS, Bennett CJ, Mebel AM, Kaiser RI (2005) Investigating the mechanism for the formation of nitrous oxide [N₂O(X¹Σ⁺)] in extraterrestrial ices. *Astrophys J* 624:436–447. <https://doi.org/10.1086/428933>
- Almeida GC, et al. (2017) Processing of N₂O ice by fast ions: implications on nitrogen chemistry in cold astrophysical environments. *Mon Not R Astron Soc* 471:1330–1340. <https://doi.org/10.1093/mnras/stx1438>
- Strobel DF, Zhu X (2017) Comparative planetary nitrogen atmospheres: Density and thermal structures of Pluto and Triton. *Icarus* 291:55–64. <https://doi.org/10.1016/j.icarus.2017.03.013>
- Mifsud DV, et al. (2022) Comparative electron irradiations of amorphous and crystalline astrophysical ice analogues. *Phys Chem Chem Phys* 24:10974–10984. <https://doi.org/10.1039/d2cp00886f>
- de Barros ALF, et al. (2017) Formation of nitrogen- and oxygen-bearing molecules from radiolysis of nitrous oxide ices implications for Solar system and interstellar ices. *Mon Not R Astron Soc* 465:3281–3290. <https://doi.org/10.1093/mnras/stw2938>
- Hudson RL, et al. (2017) Infrared spectra and band strengths of amorphous and crystalline N₂O. *J Chem Phys* 146(024304). <https://doi.org/10.1063/1.4973548>
- Koga R, et al. (2024) Mid-infrared imaging spectroscopic measurements of C₂H₄ frost simulating the outer solar system environments. *Earth Planets Space* 76(31). <https://doi.org/10.1186/s40623-024-01976-y>
- Qi W, et al. (2015) Enhanced interference pattern visibility using multislit optical superposition method for imaging-type two-dimensional Fourier spectroscopy. *Appl Opt* 54:6254–6259. <https://doi.org/10.1364/AO.54.006254>
- Dows DA (1957) Infrared spectrum of solid nitrous oxide. *J Chem Phys* 26:745–747. <https://doi.org/10.1063/1.1743396>
- Kuchta B, Eters RD (1992) The influence of molecular shapes on the relative stability of solid phases: Application to N₂O. *J Chem Phys* 97:5662–5668. <https://doi.org/10.1063/1.463774>
- Wang F, et al. (2001) Core molecular orbital contribution to N₂O isomerization as studied using theoretical electron momentum spectroscopy. *Spectrochim Acta A* 57:915–925. [https://doi.org/10.1016/s1386-1425\(00\)00335-8](https://doi.org/10.1016/s1386-1425(00)00335-8)
- Minissale M, et al. (2014) Solid state chemistry of nitrogen oxides – Part I: surface consumption of NO. *Phys Chem Chem Phys* 16:8257–8269. <https://doi.org/10.1039/c3cp54917h>
- Bergantini A, de Barros ALF, Toribio NN, Rothard H, Boduch P, da Silveira EF (2022b) Infrared spectroscopic study on swift-ion irradiation of solid N₂O-H₂O samples: Synthesis of N-O bearing species in astrophysical ices. *J Phys Chem A* 126:2007–2017. <https://doi.org/10.1021/acs.jpca.2c00768>
- Fulvio D, Baratta GA, Sivaraman B, Mason NJ, da Silveira EF, de Barros ALF, Pandoli O, Strazzulla G, Palumbo ME (2019) Ion irradiation of N₂O ices and NO₂:N₂O₄ ice mixtures: first steps to understand the evolution of molecules with the NO bond in space. *Mon Not R Astron Soc* 483:381–391. <https://doi.org/10.1093/mnras/sty3081>
- Zhao B, Hirahara Y, Li Y, Negishi S, Sasago H, Kasaba Y, Koga R, Nakagawa T, Matsuhara H, Enokidani U, Wada T (2024) Development of the broadband Fourier transform IR imaging spectrometer with common path wavefront division phase-shift interferometry for compact satellite payload. In: *Space Telescopes and Instrumentation 2024: Optical, Infrared, and Millimeter Wave*, SPIE 13092:130922X. <https://doi.org/10.1117/12.3019640>

- McKevitt JE, Beegadhur S, Ayin-Walsh L, Dixon T, Criscola F, Patadia D, Bulla S, Galinzoga J, Wadsworth B, Bornberg C, et al. (2024) Concept of operations for the Neptune system mission Arcanum. *Aeronaut J* 128(1321):469-488. <https://doi.org/10.1017/aer.2023.114>
- May TF, Decker CM, Profeta JJ, Biju R, Bayandor J (2025) 2044: A DEEP Space Odyssey. In: *AIAA SCITECH 2025 Forum*. <https://doi.org/10.2514/6.2025-1402>
- Ferreira AGM, Lobo LQ (2009) Nitrous oxide: Saturation properties and the phase diagram. *J Chem Thermodyn* 41(12):1394-1399. <https://doi.org/10.1016/j.jct.2009.06.017>

Appendix

Table 5: N_xO_y absorption bands from literature (Part 1)

Chemical species	State	Wavelength/ μm	Vibrational mode	Reference
NO	$N_2O_4/\text{cis-},\text{trans-}(\text{NO})_2$	5.29	ν_1	Bergantini et al. 2022b
N_2O_4	N_2O ice	5.35	$\nu_4+\nu_5/\nu_1$	//
N_2O_3	N_2O ice by $^{136}\text{Xe}^{23+}$ irradiation	5.40	ν_1	//
N_2O_3	N_2O ice by $^{136}\text{Xe}^{23+}$ irradiation	5.43	ν_1	//
N_2O_3	N_2O ice by $^{136}\text{Xe}^{23+}$ irradiation	5.46	ν_1	//
$N_2O_4/\text{cis-}(\text{NO})_2$	N_2O ice by $^{136}\text{Xe}^{23+}$ irradiation	5.67	$\nu_9+\text{R}/\nu_5$	//
$N_2O_4/\text{trans-}(\text{NO})_2$	N_2O ice by $^{136}\text{Xe}^{23+}$ irradiation	5.74	ν_9/ν_5	//
N_2O_4	N_2O ice by $^{136}\text{Xe}^{23+}$ irradiation	5.82	ν_7	//
NO_2	N_2O ice by $^{136}\text{Xe}^{23+}$ irradiation	6.20	ν_3	//
N_2O_3	N_2O ice by $^{136}\text{Xe}^{23+}$ irradiation	5.91	-	//
N_2O_3	N_2O ice by $^{136}\text{Xe}^{23+}$ irradiation	6.13	ν_2	//
NO_2	N_2O ice	6.21	asym stretch	//
N_2O_3	N_2O ice and $N_2O:H_2O$ mixture by $^{136}\text{Xe}^{23+}$ irradiation	6.26	ν_2	//
NO_3	$N_2O:H_2O$ mixture by $^{136}\text{Xe}^{23+}$ irradiation	6.99	tentative	//
N_2O_3	N_2O ice and $N_2O:H_2O$ mixture by $^{136}\text{Xe}^{23+}$ irradiation	7.66	ν_3	//
N_2O	N_2O ice	7.72	ν_1	//
N_2O	$N_2O:H_2O$ mixture	7.76	ν_1	//
N_2O_4	N_2O ice by $^{136}\text{Xe}^{23+}$ irradiation	7.92	ν_{11}	//
N_2O	N_2O ice and $N_2O:H_2O$ mixture	8.58	$2\nu_2$	//
O_3	N_2O ice by $^{136}\text{Xe}^{23+}$ irradiation	9.60	ν_3	//
O_3	N_2O ice by $^{136}\text{Xe}^{23+}$ irradiation	9.62	ν_3	//
N_2O_3	N_2O ice by $^{136}\text{Xe}^{23+}$ irradiation	12.74	ν_4	//
NO_2/N_2O_4	N_2O ice by $^{136}\text{Xe}^{23+}$ irradiation	13.28/13.31	ν_2/ν_{12}	//
NO	N_2O ice by H^+ irradiation	5.35	ν_1	Fulvio et al. 2019
$(\text{NO})_2$	N_2O ice by H^+ irradiation	5.67	ν_5	//
$(\text{NO})_2$	N_2O ice by H^+ irradiation	5.35	ν_1	//
NO_2	N_2O ice by H^+ irradiation	13.28	ν_2	//
NO_3	N_2O ice by H^+ irradiation	6.20	ν_3	//
NO_3	N_2O ice by H^+ irradiation	10.53	ν_1	//
NO_3	N_2O ice by H^+ irradiation	6.99	-	//
N_2O_3	N_2O ice by H^+ irradiation	12.74	ν_4	//
N_2O_3	N_2O ice by H^+ irradiation	7.66	ν_3	//
N_2O_3	N_2O ice by H^+ irradiation	6.26	ν_2	//
N_2O_3	N_2O ice by H^+ irradiation	5.46	ν_1	//
N_2O_4	N_2O ice by H^+ irradiation	13.28	ν_{12}	//
N_2O_4	N_2O ice by H^+ irradiation	7.94	ν_{11}	//
N_2O_4	N_2O ice by H^+ irradiation	5.81	ν_7/ν_5	//
N_2O_4	N_2O ice by H^+ irradiation	5.74	ν_9	//
N_2O_4	N_2O ice by H^+ irradiation	5.67	$\nu_6+\nu_{11}$	//
N_2O_5	N_2O ice by H^+ irradiation	13.59	ν_{11}	//
N_2O_5	N_2O ice by H^+ irradiation	8.05	ν_{10}	//
N_2O_5	N_2O ice by H^+ irradiation	7.46	ν_2	//
$N_2O_4; \text{NO}_2$	$\text{NO}_2:N_2O_4$ mixture	13.24–13.48	$\nu_{12}:\nu_2$	//
N_2O_3	$\text{NO}_2:N_2O_4$ mixture	12.74	ν_4	//
Unknown	$^{64}\text{Ni}^{24+}$ irradiation	7.31	-	//

Table 6: N_xO_y absorption bands from literature (Part 2)

Chemical species	State	Wavelength/ μm	Vibrational mode	Reference
NO_3	$\text{NO}_2:\text{N}_2\text{O}_4$ mixture	12.42	-	Fulvio et al. 2019
NO_3	$\text{NO}_2:\text{N}_2\text{O}_4$ mixture	10.42–10.56	ν_1	//
N_2O_4	$\text{NO}_2:\text{N}_2\text{O}_4$ mixture	7.92–7.99	ν_{11}	//
$\text{NO}_2; \text{N}_2\text{O}; \text{N}_2\text{O}_3$	$\text{NO}_2:\text{N}_2\text{O}_4$ mixture	7.67–7.65	$\nu_1:\nu_1:\nu_3$	//
NO_3	$\text{NO}_2:\text{N}_2\text{O}_4$ mixture	6.88–6.93	-	//
N_2O_3	$\text{NO}_2:\text{N}_2\text{O}_4$ mixture	6.31	ν_2	//
NO_2	$\text{NO}_2:\text{N}_2\text{O}_4$ mixture	6.19	ν_3	//
N_2O_4	$\text{NO}_2:\text{N}_2\text{O}_4$ mixture	7.91–5.83	ν_7/ν_5	//
N_2O_4	$\text{NO}_2:\text{N}_2\text{O}_4$ mixture	5.74–5.77	ν_9	//
$\text{N}_2\text{O}_4; (\text{NO})_2$	$\text{NO}_2:\text{N}_2\text{O}_4$ mixture	5.67–5.77	$\nu_6+\nu_{11}:\nu_{15}$	//
$\text{NO}; (\text{NO})_2$	$\text{NO}_2:\text{N}_2\text{O}_4$ mixture	5.34–5.35	$\nu_1:\nu_1$	//
NO	$\text{NO}_2:\text{N}_2\text{O}_4$ mixture by H^+ irradiation	5.35	ν_1	//
$(\text{NO})_2$	$\text{NO}_2:\text{N}_2\text{O}_4$ mixture by H^+ irradiation	5.67	ν_5	//
$(\text{NO})_2$	$\text{NO}_2:\text{N}_2\text{O}_4$ mixture by H^+ irradiation	5.35	ν_1	//
N_2O	$\text{NO}_2:\text{N}_2\text{O}_4$ mixture by H^+ irradiation	7.66	ν_1	//
N_2O_3	$\text{NO}_2:\text{N}_2\text{O}_4$ mixture by H^+ irradiation	7.66	ν_3	//
N_2O_3	$\text{NO}_2:\text{N}_2\text{O}_4$ mixture by H^+ irradiation	6.26	ν_2	//
N_2O_3	$\text{NO}_2:\text{N}_2\text{O}_4$ mixture by H^+ irradiation	5.46	ν_1	//
N_2O_5	$\text{NO}_2:\text{N}_2\text{O}_4$ mixture by H^+ irradiation	13.59	ν_{11}	//
N_2O_5	$\text{NO}_2:\text{N}_2\text{O}_4$ mixture by H^+ irradiation	8.05	ν_{10}	//
N_2O_5	$\text{NO}_2:\text{N}_2\text{O}_4$ mixture by H^+ irradiation	7.46	ν_2	//
N_2O_3	$\text{NO}_2:\text{N}_2\text{O}_4$ mixture by H^+ irradiation	12.74	ν_4	//
NO_2	$\text{N}_2:\text{H}_2\text{O}$ mixture	6.20	-	Barros et al. 2017
NO_3	$\text{N}_2:\text{H}_2\text{O}$ mixture	6.82	-	//
NO	$\text{N}_2:\text{H}_2\text{O}$ mixture	5.28	-	//
O_3	$\text{N}_2:\text{H}_2\text{O}$ mixture	9.60	-	//
N_2O_5	$\text{N}_2:\text{H}_2\text{O}$ mixture	7.66	-	//
N_2O_4	$\text{N}_2:\text{H}_2\text{O}$ mixture	7.67	-	//
N_2O_3	$\text{N}_2:\text{H}_2\text{O}$ mixture	5.45	-	//
N_2O_2	$\text{N}_2:\text{H}_2\text{O}$ mixture	5.66	-	//

Table 7: N_xO_y absorption bands from literature (Part 3)

Chemical species	State	Wavelength/ μm	Vibrational mode	Reference
NO	(SiO) _x substrate NO+O ₂ reaction	5.27	-	Minissale et al. 2014
cis-(NO) ₂	(SiO) _x substrate NO+O ₂ reaction	5.37	N-O s-str(a _g (1))	//
cis-(NO) ₂	(SiO) _x substrate NO+O ₂ reaction	5.63	N-O s-str(b _u (5))	//
NO ₂	(SiO) _x substrate NO+O ₂ reaction	6.23	N-O a-str	//
ONNO ₂	(SiO) _x substrate NO+O ₂ reaction	7.62	N=O s-str	//
ONNO ₂	(SiO) _x substrate NO+O ₂ reaction	5.45	N-O s-str	//
ONNO ₂	(SiO) _x substrate NO+O ₂ reaction	6.23	N-O s-str	//
ONNO ₂	Gold substrate NO+N reaction	7.63	NO ₂ deform	//
N ₂ O ₄	(SiO) _x substrate NO+O ₂ reaction	5.33	N=O str	//
N ₂ O ₄	(SiO) _x substrate NO+O reaction	5.74	NO ₂ a-str(b _{3u} (11))	//
N ₂ O ₄	(SiO) _x substrate NO+O reaction	7.96	NO ₂ a-str(b _{2u} (11))	//
N ₂ O	H ₂ O ice substrate NO+N ₂ O reaction	7.78	N=O str	//
¹⁶ O ¹⁶ O ¹⁶ O ₃	(SiO) _x substrate NO+O ₃ reaction	9.58	O-O a-str	//
¹⁸ O ¹⁸ O ¹⁶ O ₃	CO ice substrate NO+N ₂ O reaction	10.27	O-O a-str	//
NO	¹⁴ N ⁺ irradiation	5.37	NO Monomer stretch	Almeida et al. 2017
N ₂ O ₂	¹⁴ N ⁺ irradiation	5.67	On-No Antisymmetric stretch	//
N ₂ O ₄ /N ₂ O ₅	¹⁴ N ⁺ irradiation	5.75	NO stretch	//
N ₂ O ₅	¹⁴ N ⁺ irradiation	5.85	(B) Antisymmetric NO stretch	//
N ₂ O ₄	¹⁴ N ⁺ irradiation	7.94	(B _{3u}) NO stretch	//
NO ₂	¹⁴ N ⁺ irradiation	6.20	Antisymmetric stretch	//
O ₃	¹⁴ N ⁺ irradiation	9.63	Antisymmetric stretch	//
N ₂ O ₃	¹⁴ N ⁺ irradiation	6.28	NO ₂ Antisymmetric stretch	//
N ₂ O ₃	¹⁴ N ⁺ irradiation	7.65	NO ₂ Symmetric stretch	//
N ₂ O ₃	¹⁴ N ⁺ irradiation	12.76	Deformation of NO ₂ group	//
N ₂ O ₄	e ⁻ irradiation	7.93	ν_{12}	Mifsud et al. 2022